

Assessing Stagnation Conditions and Identifying Trends in Magnetized Liner Inertial Fusion

Matthew R. Gomez¹, *Member, IEEE*, Stephen A. Slutz, Patrick F. Knapp, Kelly D. Hahn, *Member, IEEE*, Matthew R. Weis, Eric C. Harding, Matthias Geissel, Jeffrey R. Fein, Michael E. Glinsky, Stephanie B. Hansen, Adam J. Harvey-Thompson, Christopher A. Jennings, Ian C. Smith, Daniel Woodbury, David J. Ampleford², *Senior Member, IEEE*, Thomas J. Awe, Gordon A. Chandler, *Member, IEEE*, Mark H. Hess, Derek C. Lamppa, *Member, IEEE*, Clayton E. Myers³, Carlos L. Ruiz, Adam B. Sefkow, *Member, IEEE*, Jens Schwarz, David A. Yager-Elorriaga, *Member, IEEE*, Brent Jones, *Member, IEEE*, John L. Porter, Kyle J. Peterson⁴, *Member, IEEE*, Ryan D. McBride⁵, *Member, IEEE*, Gregory A. Rochau, and Daniel B. Sinars, *Senior Member, IEEE*

Abstract—Magnetized Liner Inertial Fusion (MagLIF) is a magneto-inertial fusion concept, which is presently being studied on the Z Pulsed Power Facility. The concept utilizes an axial magnetic field and laser heating to produce fusion-relevant conditions at stagnation despite a peak magnetically driven implosion velocity of less than 100 km/s. Initial experiments demonstrated the viability of the concept but left open questions about the amount of laser energy coupled to the fuel and the role that mix played in the stagnation conditions. In this paper, simple methodologies for estimating the laser energy coupled to the fuel and determining the stagnation pressure and mix are presented. These tools enabled comparisons across many experiments to establish performance trends, as well as allow

comparisons with 2-D magnetohydrodynamics simulations. The initial experiments were affected by low laser energy coupling (0.2–0.6 kJ), which resulted in reduced neutron yields ($1\text{--}2 \times 10^{12}$). In addition, all early experiments utilized mid-Z (aluminum) fuel-facing components. Mixing from these components had a significant impact on stagnation and increased with laser energy. Lower neutron yields ($1\text{--}3 \times 10^{11}$) were measured with higher laser coupling (0.8–1.2 kJ), which significantly deviated from the predicted scaling. When all fuel-facing components were made from a low-Z material (beryllium), neutron production increased (3.2×10^{12}) and scaled as expected with laser energy; experimental yields were approximately 40% of simulated yields. In addition, roughly I^4 yield scaling was observed in experiments, where the load current was varied from 16–18 MA. These results represent the first step in experimental demonstration of stagnation performance scaling with input parameters in MagLIF.

Index Terms—High-energy density physics, magnetic direct drive, Magnetized Liner Inertial Fusion (MagLIF), magnet-inertial fusion, Z Pulsed Power Facility.

Manuscript received October 24, 2018; accepted December 20, 2018. This work was supported by the Sandia National Laboratories, a multi-mission laboratory managed and operated by the National Technology & Engineering Solutions of Sandia, LLC., a wholly owned subsidiary of Honeywell International, Inc., U.S. Department of Energy's National Nuclear Security Administration, under Contract DE-NA0003525. The work of D. Woodbury was supported by the SSGF Program under Grant DE-NA0003864. The review of this paper was arranged by Senior Editor S. J. Gitomer. (*Corresponding author: Matthew R. Gomez.*)

M. R. Gomez, S. A. Slutz, P. F. Knapp, M. R. Weis, E. C. Harding, M. Geissel, J. R. Fein, M. E. Glinsky, S. B. Hansen, A. J. Harvey-Thompson, C. A. Jennings, I. C. Smith, D. J. Ampleford, T. J. Awe, G. A. Chandler, M. H. Hess, D. C. Lamppa, C. E. Myers, C. L. Ruiz, J. Schwarz, D. A. Yager-Elorriaga, B. Jones, J. L. Porter, K. J. Peterson, G. A. Rochau, and D. B. Sinars are with Sandia National Laboratories, Albuquerque, NM 87185 USA (e-mail: mrgomez@sandia.gov).

K. D. Hahn was with Sandia National Laboratories, Albuquerque, NM 87185 USA. She is now with the Lawrence Livermore National Laboratory, Livermore, CA 94550 USA.

D. Woodbury was with Sandia National Laboratories, Albuquerque, NM 87185 USA. He is now with the Department of Physics, University of Maryland at College Park, College Park, MD 20742 USA.

A. B. Sefkow was with Sandia National Laboratories, Albuquerque, NM 87185 USA. He is now with the Laboratory for Laser Energetics, University of Rochester, Rochester, NY 14623 USA.

R. D. McBride was with Sandia National Laboratories, Albuquerque, NM 87185 USA. He is now with the Department of Nuclear Engineering and Radiological Sciences, University of Michigan at Ann Arbor, Ann Arbor, MI 48109 USA.

Color versions of one or more of the figures in this paper are available online at <http://ieeexplore.ieee.org>.

Digital Object Identifier 10.1109/TPS.2019.2893517

I. INTRODUCTION

EFFICIENT thermonuclear fusion requires generating plasma at high enough temperature and sufficient density and confining it for a long enough duration. In magnetic confinement fusion schemes, magnetic fields on the order of 10 T are used to confine meter-scale, low-density plasma ($10^{20}/\text{m}^3$), ideally for seconds to hours [1]–[3]. Inertial confinement fusion schemes typically utilize fast implosions to generate 10- μm scale, high-density plasma ($10^{32}/\text{m}^3$) for tens to hundreds of picoseconds [4]–[6]. Magneto-inertial fusion concepts sit in the broad space between inertial and magnetic confinement, relying both on applied magnetic fields and on compression of the fuel [7]–[10]. Some magneto-inertial fusion concepts are closer to magnetic confinement fusion, and they rely on relatively low-density plasma confined for microsecond to millisecond duration. Others are closer to inertial confinement fusion, with relatively high-density

plasma confined for hundreds of picoseconds to tens of nanoseconds.

Magnetized Liner Inertial Fusion (MagLIF) is a magneto-inertial fusion concept that sits closer to the traditional inertial confinement fusion region of phase space [11], [12]. In MagLIF, gaseous fusion fuel at roughly 1 kg/m^3 is contained in an approximately 10-mm-tall, 5-mm-diameter metal can with 0.5-mm-thick walls, referred to as a “liner,” as shown in Fig. 1. An axial magnetic field in the tens of tesla range is applied to the liner slowly enough (few ms rise time) so that it can diffuse through the conducting metal walls and surrounding electrodes [14]. A terawatt-class, 527-nm laser [15], [16] enters the target axially through a few- μm thick plastic window and deposits hundreds to thousands of joules into the fuel, heating it to hundreds of eV. The axial magnetic field limits radial thermal conduction losses to the substantially colder liner wall. The nearly 20-MA current from the Z machine [17], [18] flows through the liner, generating a self-magnetic field, which produces a radially inward force. The liner implosion is typically timed such that the laser heats the fuel just as the inner surface of the liner begins to move inward [11], [19]. This maximizes the PdV work the liner can do on the fuel while minimizing the time that the fuel can lose energy through conduction and radiation losses. The fuel temperature increases quasi-adiabatically to several keV by stagnation, and the initial magnetic field is amplified through the magnetic flux compression to thousands of tesla. The increased field is necessary to continue to limit the thermal conduction losses as the plasma pressure increases, but it is also critical to trap the charged fusion products, so their energy can be deposited in the fuel.

The initial MagLIF experiments demonstrated the fundamental requirements for successful magneto-inertial fusion. Thermonuclear neutron generation was inferred from isotropic, Gaussian primary neutron spectra [20]. Highly magnetized fusion products at stagnation were inferred from both the primary-to-secondary neutron yield ratio and the secondary neutron spectra [21]–[23]. Fusion-relevant temperatures were inferred from high-energy X-ray spectra as well as the primary neutron spectra [20], [24]. These experiments also demonstrated that the MagLIF concept is critically dependent on both magnetization and laser heating to produce significant fusion yield.

However, several puzzles associated with the initial MagLIF experiments have persisted. The 2-D magnetohydrodynamics simulations predicted that primary deuterium–deuterium (DD) neutron yields approaching 10^{13} were possible for this configuration, but the observed yields were nearly an order of magnitude lower ($1\text{--}2 \times 10^{12}$) [19], [20]. In addition, an experiment with higher initial fuel density (1.4 versus 0.7 kg/m^3) had almost no measurable yield or detectable fuel stagnation column, despite a prediction that it would perform similar to the lower density experiments [20]. The leading hypothesis to explain these discrepancies was that the amount of laser coupling was substantially lower than the expected [19], [20], [25]. This led to subsequent experiments, in which the target was modified in a way expected to increase the laser energy coupled to the fuel; however, those targets

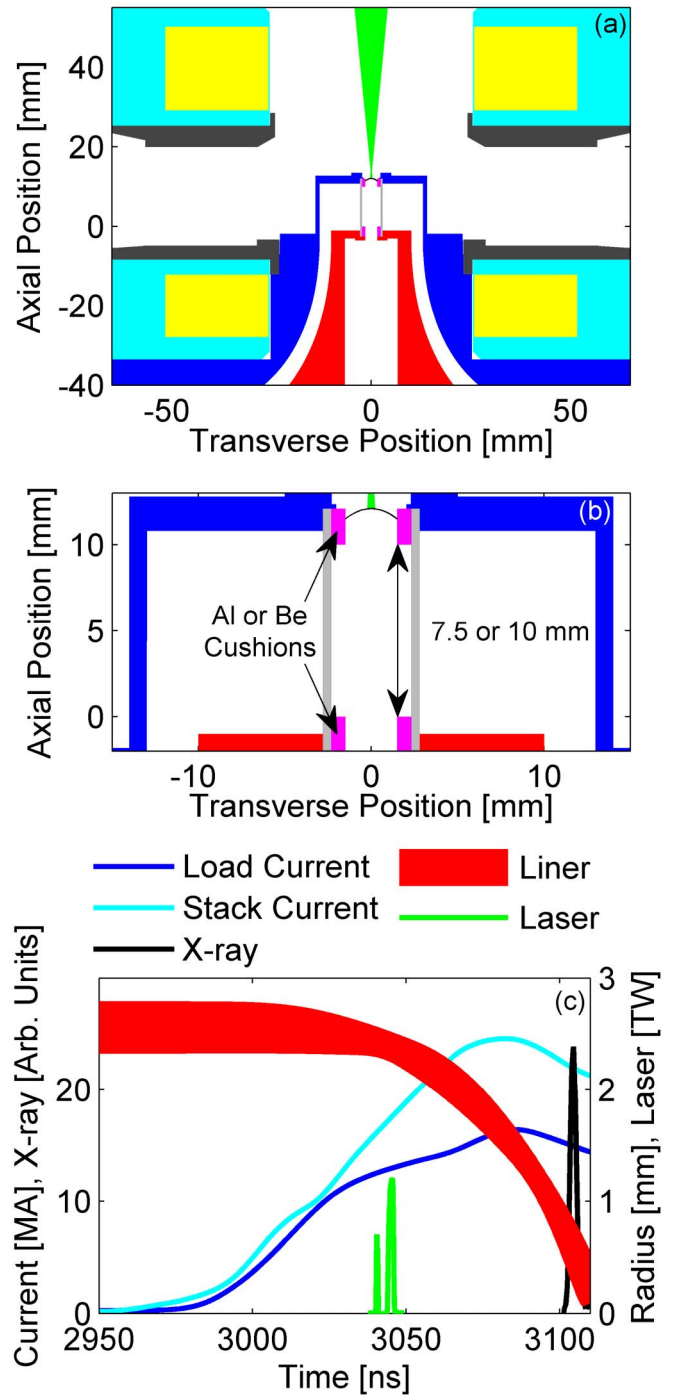


Fig. 1. (a) Cross section of the load region. Blue regions: anode; red regions: cathode; teal and yellow regions: coil footprint and windings, and green regions: laser beam path. The target was located axially between two magnetic field coils, which simultaneously allowed the magnetization of the target and X-ray diagnostic access in the radial direction. The laser entered the target axially through the bore of the top coil. The current was delivered to the target via an axially extended transmission line, which passed through the bore of the bottom coil. (b) Cross section of the target. The cushions [13], shown in magenta, were made from either beryllium or aluminum. The axial distance between the cushions was either 7.5 or 10 mm. (c) Plot of the load and stack current, laser pulse, stagnation X-ray emission, and simulated liner trajectory from z2851.

produced significantly lower neutron yields ($2\text{--}3 \times 10^{11}$) than the original experiments [26]. This led to speculation that the laser energy coupled to the fuel increased, but it also caused

an increase in radiative losses due to nonfuel mixing into the plasma.

To better understand the results of the initial MagLIF experiments, a methodology to assess the laser energy coupled to the fuel based on surrogate experiments was developed. In addition, a process for assessing the stagnation pressure and fuel mix level based on the observed X-ray and neutron emission was established. These procedures are described in Sections II and III, respectively. Additional experiments varying the target dimensions and/or materials as well as the laser timing and/or energy were conducted to better understand the impact of laser energy coupling and induced mix on target performance. The analysis techniques described in Sections II and III are applied to both the new data sets and those from the original experiments in Section IV, and conclusions are given in Section V.

II. ESTIMATING LASER ENERGY COUPLED TO THE FUEL

The laser energy coupled to the fuel has not been directly measured on any MagLIF experiment. Diagnosing the laser preheat is challenging due to the low amount of energy coupled and the limited diagnostic access. With around 1 kJ coupled, the peak electron temperature would be on the order of 1 keV, with much of the fuel below 200 eV. X-ray diagnosis from the radial direction is restricted by the beryllium liner surrounding the fuel, which at the time of preheat is less than 1% transmissive for X-rays below 2.2 keV. Fuel doped with argon produces spectral lines around 3 keV, which could aid in diagnosis of the fuel conditions during the laser heating stage [26]. However, the argon concentration required (approximately, 0.1% atomic) significantly increases the radiative losses throughout the implosion. The resulting reduction in fuel temperature, and consequently neutron yield, would be sufficiently perturbative that this technique could not be employed on integrated experiments. In addition, for the temperatures produced during the laser heating stage, argon K-shell emission would be strongly emitted from only the hottest region of the plasma, while the bulk of the fuel would be too cool to produce significant emission. The laser energy coupled to the fuel would be significantly underestimated based on this emission. Efforts to diagnose the fuel temperature axially through the laser entrance hole (LEH) window appear promising but are in the early stages of development.

Experiments using surrogate targets [27], [28] have been successful in diagnosing energy coupled to the fuel [29]; however, these targets require diagnostic access windows that cannot be included in the experiments on the Z Facility. Experiments with these surrogate targets have been used to develop new laser heating configurations [30] and can be used to predict/postdict the laser energy coupled in MagLIF experiments [29]. This method is limited by the requirement that many previous laser/fuel/window configurations need to be tested to understand the laser coupling for each case. This path is being pursued, but it is in direct competition for resources with efforts to develop improved laser configurations for upcoming experiments.

While the energy coupled to the fuel by the laser has not been measured in any MagLIF experiment, the energy

exiting the laser is measured on every MagLIF experiment. A method to estimate the laser energy coupled to the fuel was developed based on these measurements and an energy balance that accounts for the known loss mechanisms. The procedure accounts for the energy lost in the optical chain between the laser energy measurement and the target in the Z Facility vacuum chamber, as well as the energies backscattered from the target and absorbed in the window—as determined in surrogate experiments—to determine the energy that reaches the fuel.

This analysis, described in detail in the following, was applied to the experiments listed in Table I. The energy absorbed in the fuel was around 1 kJ in targets with 1.5- μm -thick LEH windows and 0.5 kJ in targets with 3- μm -thick LEH windows. The energy absorbed in the window was around 0.7 kJ for targets with 1.5- μm windows and 1.2 kJ for targets with 3- μm windows. The energy lost to stimulated Brillouin scattering (SBS) was around 0.3 kJ for targets with 1.5- μm windows and 0.6 kJ for targets with 3- μm windows. Note that these values apply to the experiments with approximately 2 kJ of laser energy; the values were all roughly doubled for the experiment with 4 kJ.

The laser energy and pulse shape were measured on each experiment with a diode that monitors a small amount of energy picked off from the main beam. The diode was calibrated based on preshot and/or postshot laser pulses into a calorimeter. The calorimeter had a calibration uncertainty of $\pm 3\%$. The digitizers used to measure the diode and calorimeter signals had calibration uncertainties of $\pm 2\%$. Combining these uncertainties with the uncertainty in the beam fraction picked off led to an assumed total uncertainty in the energy measurement of $\pm 5\%$. Table I contains the laser energy for each MagLIF experiment in this paper.

Over the 72-m translation from the measurement of the laser energy to the Z Facility vacuum chamber, the beam encountered 10 optics, including lenses, windows, a beam splitter, and a mirror. The optimal efficiencies of these optics ranged between 95.1% and 99.7% with a net optimal transmission through the chain of 86.1%. The efficiency of these optics can be degraded via several mechanisms (e.g., laser damage sites and absorption of humidity), leading to reduced transmission. The efficiency of the optical chain was not measured for each experiment, but it was estimated that the efficiency was typically between 83% and 86%, with low probability that the efficiency was below 79%. Based on this, the probability distribution function was assumed to be flat from 83% to 86% and half of a Gaussian distribution with a center at 83% and $\sigma = 2\%$. The energy reaching the target was determined by

$$E_{\text{tp}} + E_{\text{tm}} = (E_{\text{pre}} + E_{\text{main}}) * f_{\text{OC}} \quad (1)$$

where E_{tp} and E_{tm} were the prepulse and main pulse energies on target, respectively, E_{pre} and E_{main} were the measured energies of the prepulse and main pulse, respectively, and f_{OC} was the fractional transmission of the optical chain. Using the probability distribution of the measured laser energy and the fractional transmission of the optical chain, the energy reaching the target was estimated, examples of which are shown in Fig. 2.

TABLE I
LASER CONFIGURATIONS

Shot	z2583 ^{ab}	z2591 ^{ab}	z2613 ^{ab}	z2707 ^a	z2708 ^a	z2758 ^c	z2768 ^d	z2769 ^{de}	z2839	z2850 ^b	z2851 ^b	z2852 ^b	z2985
Fuel Density [kg/m ³]	1.4	0.7	0.7	0.7	0.7	0.7	0.7	0.7	0.7	0.7	0.7	0.7	0.7
LEH foil thick. [μm]	3.26	3.26	3.60	1.85	1.85	1.52	1.89	1.89	1.52	3.60	3.60	3.60	1.89
LEH window deflect. [mm]	0.6	0.6	0.6	0.6	0.6	0.474	0.588	0.588	0.738	0.688	0.688	0.688	0.588
LEH window thick. [μm]	2.75	2.80	3.09	1.47	1.47	1.27	1.51	1.51	1.13	2.97	2.97	2.97	1.51
Prepulse energy [kJ]	0.61	0.39	0.46	0.32	0.40	0.37	0.47	0.35	0.44	0.42	0.40	0.46	0.62
Main pulse energy [kJ]	2.46	2.04	1.95	1.79	2.29	1.82	2.50	3.98	2.34	2.33	2.10	2.27	2.12
Main pulse energy on target [kJ]	2.04 (+0.11) (-0.11)	1.70 (+0.09) (-0.09)	1.62 (+0.09) (-0.09)	1.49 (+0.08) (-0.08)	1.90 (+0.11) (-0.10)	1.51 (+0.08) (-0.08)	2.08 (+0.11) (-0.12)	3.31 (+0.18) (-0.18)	1.94 (+0.11) (-0.11)	1.93 (+0.11) (-0.11)	1.75 (+0.10) (-0.10)	1.88 (+0.10) (-0.10)	1.76 (+0.10) (-0.10)
SBS backscatter energy [kJ]	0.77 (+0.20) (-0.21)	0.58 (+0.16) (-0.16)	0.60 (+0.16) (-0.17)	0.29 (+0.07) (-0.07)	0.38 (+0.09) (-0.09)	0.27 (+0.06) (-0.06)	0.43 (+0.10) (-0.10)	0.67 (+0.17) (-0.16)	0.32 (+0.07) (-0.07)	0.69 (+0.18) (-0.19)	0.62 (+0.17) (-0.17)	0.67 (+0.18) (-0.19)	0.36 (+0.09) (-0.09)
Energy delivered to fuel [kJ]	0.48 (+0.27) (-0.31)	0.50 (+0.17) (-0.26)	0.40 (+0.12) (-0.28)	0.87 (+0.26) (-0.24)	1.12 (+0.33) (-0.31)	0.97 (+0.24) (-0.27)	1.20 (+0.36) (-0.32)	1.88 (+0.60) (-0.49)	1.38 (+0.28) (-0.40)	0.52 (+0.16) (-0.32)	0.46 (+0.15) (-0.29)	0.51 (+0.15) (-0.32)	1.02 (+0.30) (-0.28)
Energy abs. in LEH window [kJ]	1.32 (+0.23) (-0.23)	0.97 (+0.19) (-0.17)	1.07 (+0.18) (-0.16)	0.58 (+0.23) (-0.25)	0.72 (+0.30) (-0.32)	0.58 (+0.26) (-0.24)	0.82 (+0.33) (-0.34)	0.96 (+0.54) (-0.52)	0.61 (+0.39) (-0.28)	1.13 (+0.21) (-0.19)	1.04 (+0.19) (-0.18)	1.15 (+0.20) (-0.19)	0.89 (+0.28) (-0.29)

The laser and target parameters relevant to the laser energy deposition estimation are listed. The final LEH window thickness was estimated assuming a bubble shape described by (3) and has an assumed uncertainty of ± 0.1 μm. The prepulse and main pulse energies have a $\pm 5\%$ uncertainty. Unless otherwise noted, the delay between the prepulse and the main pulse was approximately 4 ns

^aExperiments in which the LEH window deflection was estimated rather than measured

^bExperiments in which the initial LEH window deflection was produced at 120 PSI

^cExperiments in which the initial LEH window deflection was produced at 45 PSI

^dExperiments in which the LEH window thickness was measured after deformed into a bubble, both with and without pressure

^eThe main pulse duration was increased to 4 ns and the delay between prepulse and main pulse was reduced to approximately 2 ns.

For each MagLIF experiment, the window foil thickness was characterized prior to being pressurized. When pressurized, the window plastically deformed into a bubble. The exact shape of the bubble was difficult to measure, but the height of the apex of the window was typically characterized. Over the range of window thicknesses and differential pressures tested, the height of the apex of the bubble was reasonably described by

$$z_0 \approx 1.5 - 30 \times \frac{T}{P} \quad (2)$$

where z_0 is the offset in mm, T is the initial thickness of the foil in μm, and P is the deforming pressure in psi. This relationship was used to estimate the height of the apex of the bubble in experiments in which it was not measured. For a limited number of experiments, the height of the bubble apex was measured with and without a pressure differential, which allowed an estimation of the impact of elastic deformation of the window in addition to the plastic deformation. On average, the height of the apex of the window increased by 14.3% due to the elastic deformation. This factor was applied to experiments, in which the apex height was not measured

while pressurized. In experiments in which the window was plastically deformed with a different pressure than used on the experiment, the elastic deformation factor was scaled by the ratio of the experimental pressure to the initial deforming pressure.

The expected shape of a thin membrane with a pressure differential is given by

$$z(r) = z_0 \left(1 - \frac{r^2}{R^2} \right) \quad (3)$$

where z is the axial offset as a function of radial position, r , z_0 is the axial offset at the apex, and R is the outer radius of the foil [31]. Assuming this shape, conservation of the foil volume, and that the stretching of the membrane resulted in a uniform change in thickness, the thickness of the foil after stretching was estimated for each experiment. For a few experiments, extra resources were devoted to measuring the postpressurization window thickness, thus enabling a check on the above-mentioned approximation. The estimated foil thicknesses matched the measured thickness for the nominally 3.5-μm foils, but the nominally 1.8-μm foils required a correction of -5.8% to the estimated foil thickness.

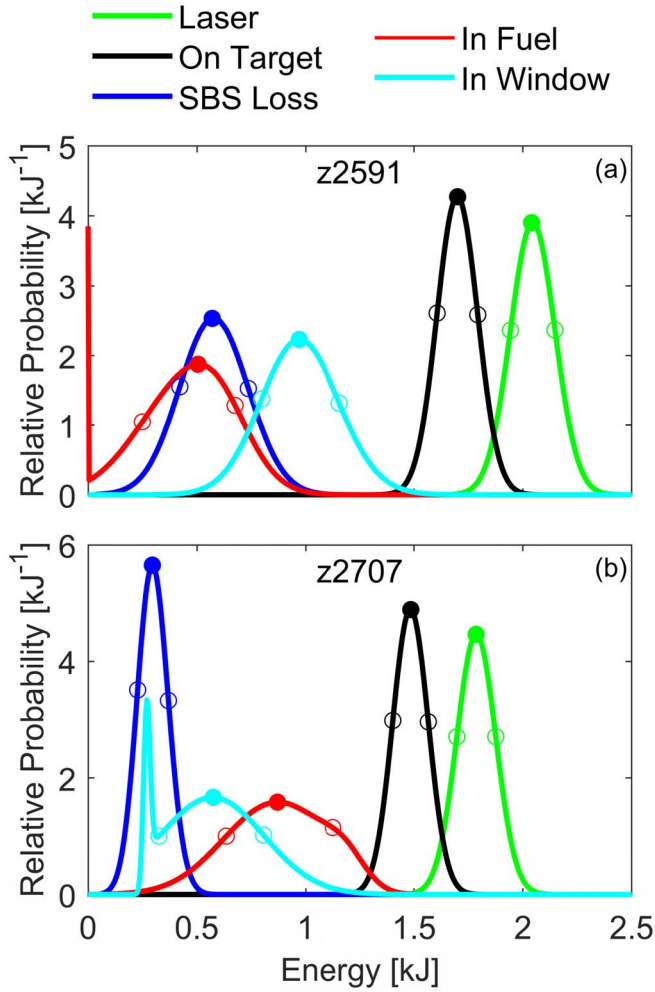


Fig. 2. Plots of the distributions of energy at the output of the laser (Laser), the energy that reached the target (On Target), the energy lost to SBS backscatter (SBS loss), the energy absorbed in the fuel (In Fuel), and the energy absorbed in the window (In Window) for z2591 (3.5- μ m-thick LEH window) and z2707 (1.8- μ m-thick LEH window). The most likely value for each distribution is marked with a solid circle, and the open circles mark the edges of the central 68.3% of each distribution. The most likely value was chosen to be the peak of the distribution within the central 68.3% of the distribution. The peak in the “In Fuel” distribution for (a) z2591 was caused by cases, where none of the main pulse energy reached the fuel. The peak in the “In Window” distribution for (b) z2707 was caused by cases, where none of the main pulse energy was absorbed in the window.

The laser pulse shape consisted of an approximately 0.5-kJ, 0.5-ns prepulse and a 2–4-kJ, 2–4-ns main pulse, which were separated by 2–4 ns. The purpose of the prepulse was to heat the LEH window to roughly 1 keV and allow it to rarefy, so the window plasma would be more transmissive for the main pulse.

Laser plasma instabilities, such as SBS and stimulated Raman scattering (SRS), could produce intensity-dependent losses of laser energy in MagLIF [28]. In the early experiments, no beam smoothing was used, so the beam quality was poor, as shown in Fig. 3. As a result, the spot size of the beam was poorly defined. Lower and upper bounds on the effective beam area were estimated at 0.028 and 0.22 mm², respectively. These limits were determined by the area containing the

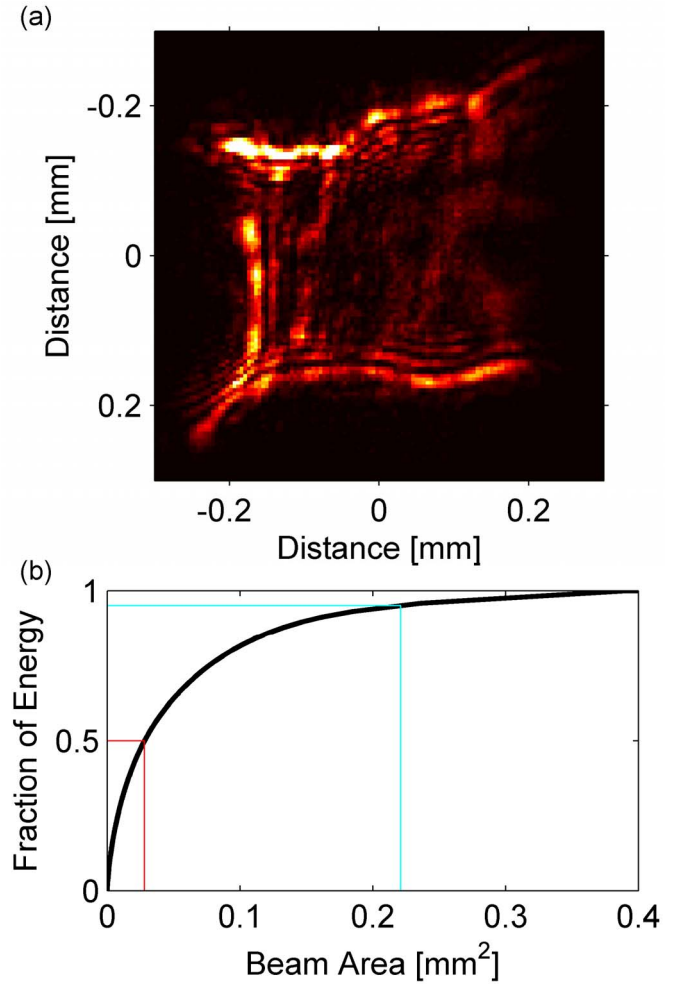


Fig. 3. (a) Image of the unconditioned beam spot at 3.5-mm past focus, as was incident on the LEH foil in these MagLIF experiments. The beam was roughly 0.45-mm square with significant intensity modulations. (b) Plot of the energy contained as a function of area for the image in (a). The area containing 50% of the beam energy was 0.028 mm² and the area containing 95% of the beam energy was 0.22 mm², as shown by the red and cyan lines, respectively.

brightest 50% and 95% of the beam, respectively. Based on these limits, the intensity of the beam was estimated to be between 4×10^{14} and 3×10^{15} W/cm², and in this regime, SBS should be important, while SRS may not [28].

Measurements with surrogate LEH window targets as well as gas cell targets containing 0.7-kg/m³ deuterium were used to estimate the fraction of energy backscattered by SBS [27], [28]. As shown in Fig. 4(a), the SBS backscatter from the gas cell increased with window thickness, ranging from approximately 20% to 40% of the main pulse energy. The uncertainty in the measurement was determined by combining the scatter of the measured values and the 20% uncertainty in the energy inferred by the SBS measurement technique. The measurements of SBS backscatter from LEH window surrogate targets had additional uncertainty due to a steep gradient in the diagnostic response with wavelength (which was resolved prior to conducting the gas cell measurements). The backscatter from the window material increased from

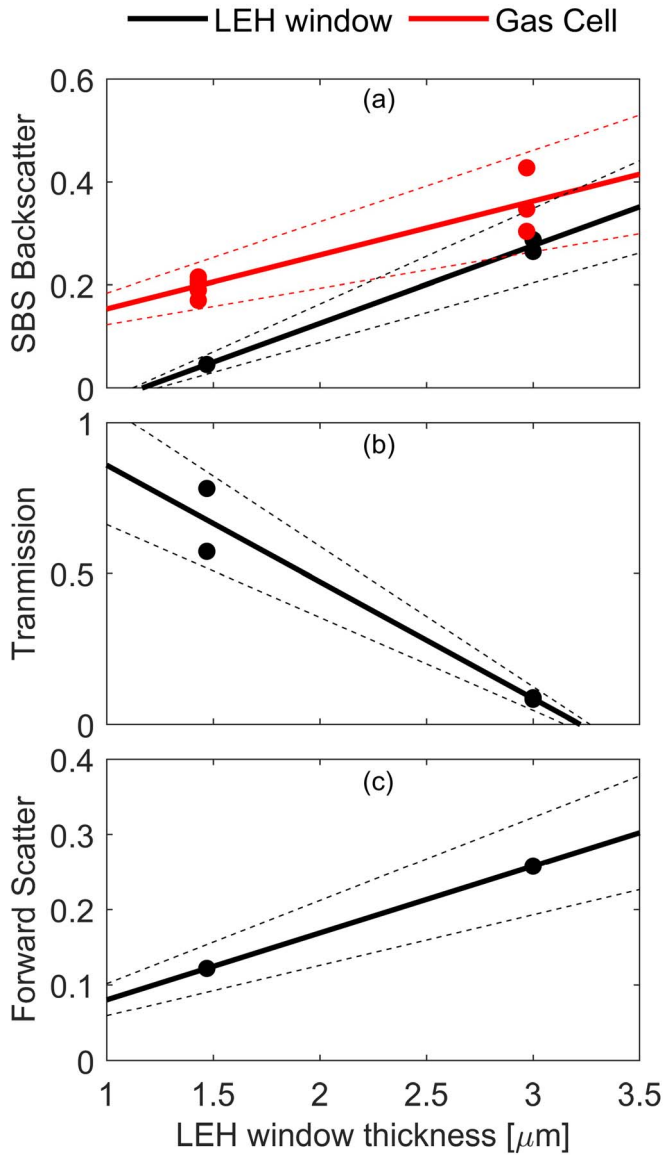


Fig. 4. Plots of the measured energy fraction in (a) SBS backscatter, (b) window transmission, and (c) large angle forward scatter for experiments with a surrogate LEH window and a D₂ gas cell (only SBS backscatter). The measured points are plotted as solid dots, a best fit to each data set is plotted as a thick solid line, and the uncertainty in the fits are plotted as the thin dashed lines.

approximately 5% to 30% of the main pulse energy over the range of window thicknesses tested. The difference between the gas cell scattering measurements and the window scattering measurements was used to estimate the scattering from the fuel in isolation.

A similar measurement technique was used to estimate the SRS backscatter from gas cells containing 0.7-kg/m³ deuterium with 1.5- and 3-μm-thick LEH windows. The measured SRS backscatter energy was less than 1 J in all experiments. Low levels of SRS were expected in these experiments given the density of the fuel (5%–10% of the critical density of the laser) and the estimated laser intensity [28]. Given the small fraction of energy scattered via SRS, losses due to SRS were ignored in this analysis.

Both the transmitted and the forward scattered energy (energy that passed through the LEH window but was scattered outside of the nominal beam cone) were determined as a function of window thickness in measurements with a surrogate LEH window. Window transmission decreased with increasing window thickness, with approximately 70% transmission of the main pulse energy for 1.5-μm-thick polyimide and under 10% transmission for 3-μm-thick polyimide, as shown in Fig. 4(b). The uncertainty in the transmission measurement was a combination of the scatter in the measured values and approximately 7% uncertainty in the measurement due to 5% uncertainty in each calorimeter-based energy measurement. The forward scattered fraction was determined with a similar diagnostic technique as the SBS backscatter, and it had a similar uncertainty due to the steep diagnostic response as a function of wavelength. The forward scattered energy was around 10% of the main pulse energy for a 1.5-μm-thick window and around 25% for a 3-μm-thick window, as shown in Fig. 4(c). The majority of the forward scattered energy was contained within an f-number of 3.

The energy absorbed in the fuel was estimated by

$$E_{\text{Fuel}} = E_{\text{tm}} * (f_{\text{tr}}(T_w) + f_{\text{FWD}}(T_w) - f_{\text{SBSf}}(T_w)) \quad (4)$$

where f_{tr} and f_{FWD} are the fractions of incident energy transmitted through and forward scattered from the LEH window, respectively, T_w is the thickness of the LEH window after deformation, and f_{SBSf} is the fraction of incident energy backscattered by the fuel, determined by

$$f_{\text{SBSf}} = f_{\text{SBSgc}}(T_w) - f_{\text{SBSw}}(T_w) \quad (5)$$

where f_{SBSgc} and f_{SBSw} are the measured fractions of incident energy lost to SBS in the gas cell and window only experiments, respectively.

In experimental measurements with a 1-ns, 1-kJ pulse incident on a foil, no measurable energy was transmitted through the foil [28]. Typical prepulse energies were substantially lower than 1 kJ; thus, no energy from the prepulse was expected to reach the fuel. In an additional experiment with a single 0.3-kJ pulse, approximately 2% or 6 J was lost as SBS backscatter [28]. As a result, the prepulse energy was assumed to be entirely lost to absorption in the window. The energy absorbed in the window was determined by

$$E_{\text{win}} = E_{\text{tp}} + E_{\text{tm}} * (1 - f_{\text{SBSgc}}) - E_{\text{Fuel}} \quad (6)$$

which was effectively a combination of the prepulse energy that reached the target and the main pulse energy that reached the target and was not absorbed in the fuel or lost to SBS.

Since the transmission and forward scattering measurements were made with an LEH window surrogate, they did not account for the change in window dynamics when fuel tamps LEH expansion in one direction. To account for this effect, 3-D HYDRA [32] simulations were conducted of an LEH window with and without fuel, and a correction was applied to the experimental results. With fuel behind the window, the energy passing through the window decreased by 3.5% of the energy incident on the window.

HYDRA simulations were also used to account for the impact of the applied axial field. The laser experiment facility

did not have an applied magnetic field capability; thus, all the surrogate measurements neglect the impact of the 10-T axial applied B-field used in experiments on the Z Facility. The magnetic field was expected to impact transmission because it would inhibit thermal conduction in the LEH window plasma; thus, the window would retain more energy and become transmissive earlier. HYDRA simulations conducted with and without an applied B-field indicated the energy transmitted through the window was increased by a negligible amount. The smaller than expected change was a result of the high-intensity regions of the beam [see Fig. 3(a)] rapidly penetrating through the foil in the simulation.

While this energy balance methodology provides a reasonable approximation of the energy coupled to the fuel, several factors were neglected because they could not be readily estimated. Energy absorbed by the window material could be radiated into the target and absorbed by the fuel. Similarly, energy absorbed by the window material could be carried into the fuel through mix. Neither of these effects was accounted for in this analysis; both would increase the energy in the fuel, but the impact would likely be relatively small. In addition, some laser energy could penetrate through the fuel and exit the bottom of the target, which would decrease the energy in the fuel.

An alternate method for inferring the energy deposited in the fuel using shadowgraphy of the laser blast wave in experiments with surrogate targets in a separate chamber is under development [29]. The energy inferred using the blast wave methodology for laser and target configurations similar to the ones listed in Table I was around 0.1–0.2 kJ higher than the energy inferred with the energy balance analysis. The blast wave methodology was sensitive to energy introduced to the fuel through radiation from and mixing of the window material, which could explain the discrepancy. Note the axial extent of the blast wave in these experiments was typically similar to the target length, indicating the energy exiting the bottom of the target should be minimal; the one possible exception was the experiment with 4 kJ, where the energy exiting the target could have been significant. As a result, the energy absorbed in the fuel from the energy balance analysis was likely a slight underestimate in most cases. Note that the conclusions that follow are not significantly impacted by a systematic offset in inferred energy.

III. DIAGNOSING STAGNATION CONDITIONS

The set of stagnation measurements for each MagLIF experiment changes (as new diagnostics are developed and based on the objectives of the campaign), but a core set of diagnostics are typically fielded. These diagnostics are used to infer primary neutron yield, burn-averaged ion temperature, hot fuel volume, burn duration, and X-ray yield. These quantities can be combined with a model of the stagnation column to estimate the fuel pressure and the mix fraction.

The primary neutron yield isotropy was measured using indium-activation samples fielded at several locations around the target [23]. These MagLIF experiments utilized the deuterium gas as the fusion fuel; thus, the primary neutron energy

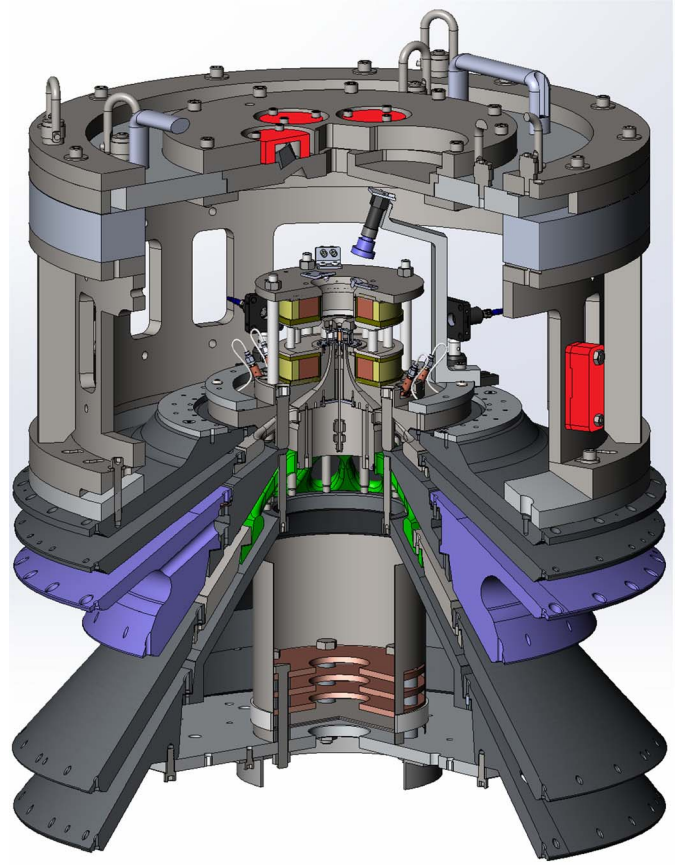


Fig. 5. Cross section of the solid model of the load region. The locations of three indium activation sample holders at a polar angle of 20° and one indium activation sample at a polar angle of 90° are highlighted in red areas. Neutron scattering off the several cm of metal in the line of sight from the source to the samples significantly impacted the measured signals. MCNP modeling was used to account for the complex scattering environment on the Z Facility.

was approximately 2.45 MeV. The measurements utilized the $^{115}\text{In}(n,n')^{115\text{m}}\text{In}$ reaction, which has a 336-keV energy threshold. $^{115\text{m}}\text{In}$ decays with a half-life of 4.5 h by emitting 336-keV gamma rays that were detected by a set of absolutely calibrated, high-purity germanium detectors. A total of nine indium activation samples were typically fielded within the vacuum chamber, as shown in Fig. 5. Samples were located at polar angles of 20° , 90° , and 170° , with three azimuthal positions for each polar angle. There was significant neutron scattering in the load region; thus, the activation measurements were corrected using a detailed Monte Carlo N-particle (MCNP) [33] model of the hardware surrounding the target and activation samples. The uncertainty in this MCNP-based correction was the dominant factor in the $\pm 20\%$ total uncertainty in the primary neutron yield. Typically, the primary yield was isotropic; the differences between the yields inferred from all the samples matched one another to within the uncertainty in the individual measurements.

The burn-averaged ion temperature was determined from a forward-fit to the primary neutron signal measured with the neutron time-of-flight (nTOF) detectors. Five nTOF detectors are fielded at the Z Facility; two are located 9.44 and 11.46 m

from the source at a polar angle of 78° and an azimuthal location of 270° , one is 25.1 m from the source at a polar angle of 78° and an azimuthal angle of 50° , and two are 6.90 and 7.86 m from the source at a polar angle of 180° [34].

The reported ion temperatures were inferred from the signal recorded by the detector located at 9.44 m since it had superior collimation; thus, the impact of neutron scattering on the signal was less than for the other detectors. Ion temperatures inferred from the signals recorded by the other detectors produced similar results, typically within the uncertainty in the value inferred from the 9.44-m detector. The ion temperature was determined using the Ballabio model [35] with additional corrections, as described in [36]; the model included corrections for the light output of the nTOF scintillator and the instrument response function. Approximately, the first two-thirds of the temporal duration of the primary neutron signal was fit using this model to determine the ion temperature. The later-time (low-energy) signal was not included in the fit due to broadening by neutron scattering in the line of sight. Given the relatively low implosion velocity in MagLIF (70–100 km/s), residual kinetic flows were assumed to be negligible, which resulted in ion temperatures nearly identical to those determined using the traditional Brysk ion temperature model [37]. The uncertainty in the inferred ion temperature was approximately 20% and was dominated by the uncertainties in the instrument response function as well as the relatively high neutron scattering environment on the Z Facility.

The hot fuel volume was diagnosed using a time-integrated high-spatial-resolution X-ray emission imager [38]. The fuel volume was estimated by comparing the measured X-ray emission image to the expected emission from a hotspot model (described in the following).

The imager consisted of a spherically bent Ge220 crystal and a filtered image plate detector. The system was sensitive to a relatively narrow X-ray band (3123.2 ± 3.8 eV) in first order, but it reflected in multiple orders. The spectral response of the diagnostic was a combination of transmission through the beryllium liner surrounding the fuel, reflectivity and bandwidth of the crystal, transmission through the detector filtration, and absorption by the image plate detector, as shown in Fig. 6. A significant signal was expected for crystal reflection in orders 2–4. The first-order signal was significantly attenuated by the approximately 0.75-g/cm² beryllium liner surrounding the fuel [39]; beyond the fourth order, both the fuel emission and the crystal reflectivity dropped significantly, and thus, higher orders were not included in this analysis.

In the emission model, the fuel was assumed to be circular in cross section and isobaric with a temperature profile

$$T(r) = T_{\text{peak}} - (T_{\text{peak}} - T_{\text{rad}}) \left(\frac{r}{R}\right)^4 \quad (7)$$

where T_{peak} is the temperature on axis, T_{rad} is the radiation temperature, r is the radial position in the fuel, and R is the radial extent of the fuel [40]. This reduced to

$$T(r) = T_{\text{peak}} * \left(1 - 0.9 * \left(\frac{r}{R}\right)^4\right) \quad (8)$$

under the assumption that T_{rad} was 10% of T_{peak} [40]. For this analysis, T_{peak} was chosen such that the width of the

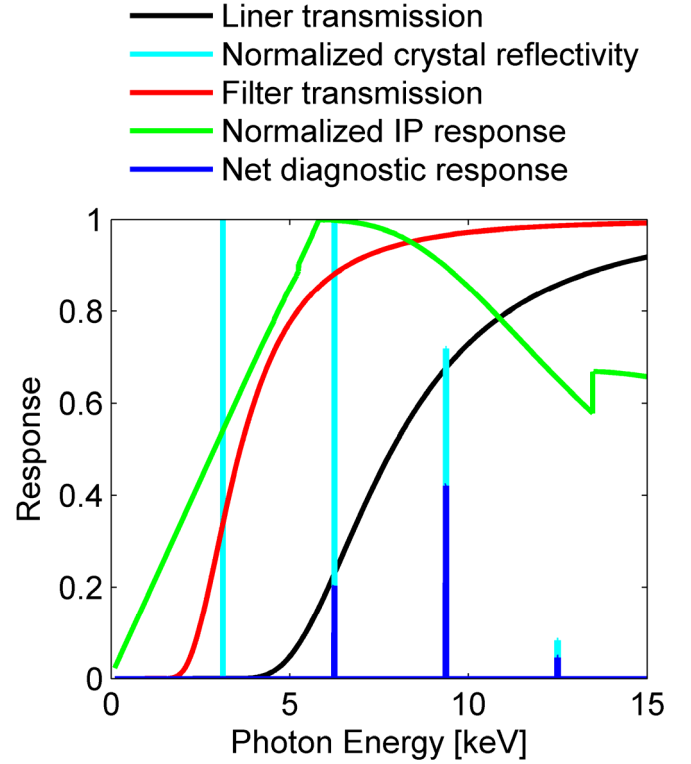


Fig. 6. Plot of the spectral sensitivities of various processes in the crystal imaging system. Note that the crystal reflectivity was normalized to the second-order reflection (6.2 keV). The first-order reflection (3.1 keV) had approximately five times greater crystal reflectivity, but due to the significant opacity of the beryllium liner, the net diagnostic response was five orders of magnitude lower than the second-order reflection. The second- and third-order reflections dominated the recorded images.

synthetic DD neutron spectrum generated with this model was consistent with the experimental ion temperature. The ions and electrons were assumed to be in temperature equilibrium due to the expected \ll ps electron-ion collision times at these conditions [20].

Emission from the fuel was modeled as a combination of bound-free (bf) and free-free (ff) emissivities

$$J(h\nu, r) = C * \sqrt{\frac{T(r)}{h\nu}} \sum_i f_i (j_{\text{bf},i}(h\nu, r) + j_{\text{ff},i}(h\nu, r)) \quad (9)$$

where $h\nu$ is X-ray photon energy, f_i represents the fractional composition of the hot fuel, and C , $j_{\text{bf},i}$, and $j_{\text{ff},i}$ are given by

$$C = \frac{0.87 * 2\sqrt{3}}{\pi} * \tau_{\text{burn}} \left(\frac{P_{\text{HS}}}{k_B}\right)^2 \frac{Z}{(Z+1)^2} \quad (10)$$

$$j_{\text{bf},i}(h\nu, r) = \frac{A_{\text{bf}} * Z_i^4}{T(r)^{3.5}} \exp\left(\frac{-h\nu}{T(r)}\right) \exp\left(\frac{R_y Z_i^2}{T(r)}\right) \quad (11)$$

$$j_{\text{ff},i}(h\nu, r) = \frac{A_{\text{ff}} Z_i^2}{T(r)^{2.5}} \exp\left(\frac{-h\nu}{T(r)}\right) \quad (12)$$

where τ_{burn} is the stagnation burn duration, P_{HS} is the fuel pressure, k_B is the Boltzmann's constant, Z_i represents the atomic number of the i th species in the fuel, R_y is the Rydberg constant, and A_{bf} and A_{ff} are the bf and ff emission coefficients, respectively. Note that the stagnation burn

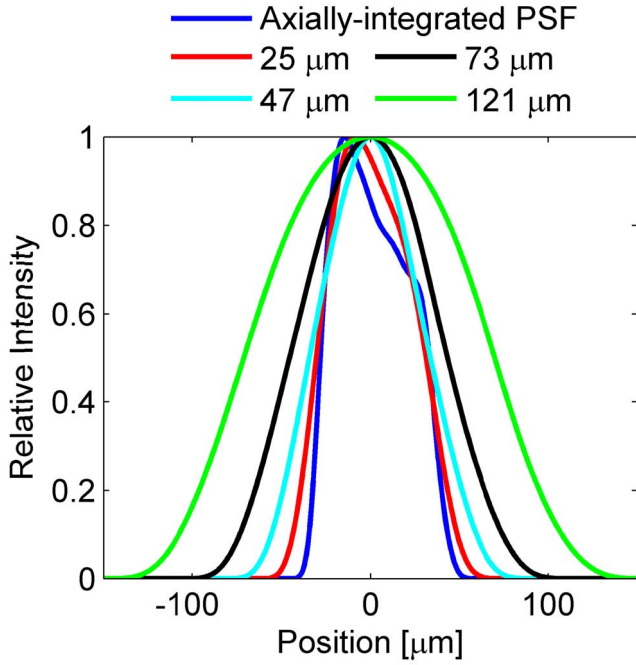


Fig. 7. Plot of the axially integrated point spread function and calculated spatial profiles for the crystal imager assuming different values of R in (8). The asymmetric point spread function of the diagnostic dominates the shape for small radius. At larger radius, the point spread function has a negligible contribution to the emission width. Note that the full-width at half maximum of emission is generally not a good representation of the source size.

duration and hot spot pressure impacted only the amplitude, and not the expected shape, of the emission profile; thus, they could be normalized out in the fuel volume calculation. The mix fraction and composition had a negligible impact on the emission profile shape over the range of values applicable to these experiments; thus, they were fixed for the plasma volume analysis.

The path-integrated image profile was generated by using (8) to populate a temperature map of the plasma cross section, applying (9)–(12) and the spectral response of the diagnostic (shown in Fig. 6) to get a normalized spatial intensity profile, and integrating along the diagnostic line-of-sight path to convert the 2-D distribution into a 1-D profile. A calculated point-spread function [38] for the crystal imager was axially integrated to generate the response in the transverse direction (see Fig. 7). This transverse response was convolved with the calculated spatial intensity profiles for a range of fuel radii to create a map of expected image profiles. An example set of profiles is plotted in Fig. 7. At each axial position in the image, the calculated image profile map was fit to the normalized measured X-ray self-emission profile, giving a value for the fuel radius.

The impact of the assumed plasma profile on the radius was investigated by testing several alternate temperature models, as shown in Fig. 8. The difference in the inferred radius for the different models was small compared to the variations in radius over the axial extent of the fuel, indicating that the analysis was not highly sensitive to the model. The average of the volume inferred with these curves was used in subsequent

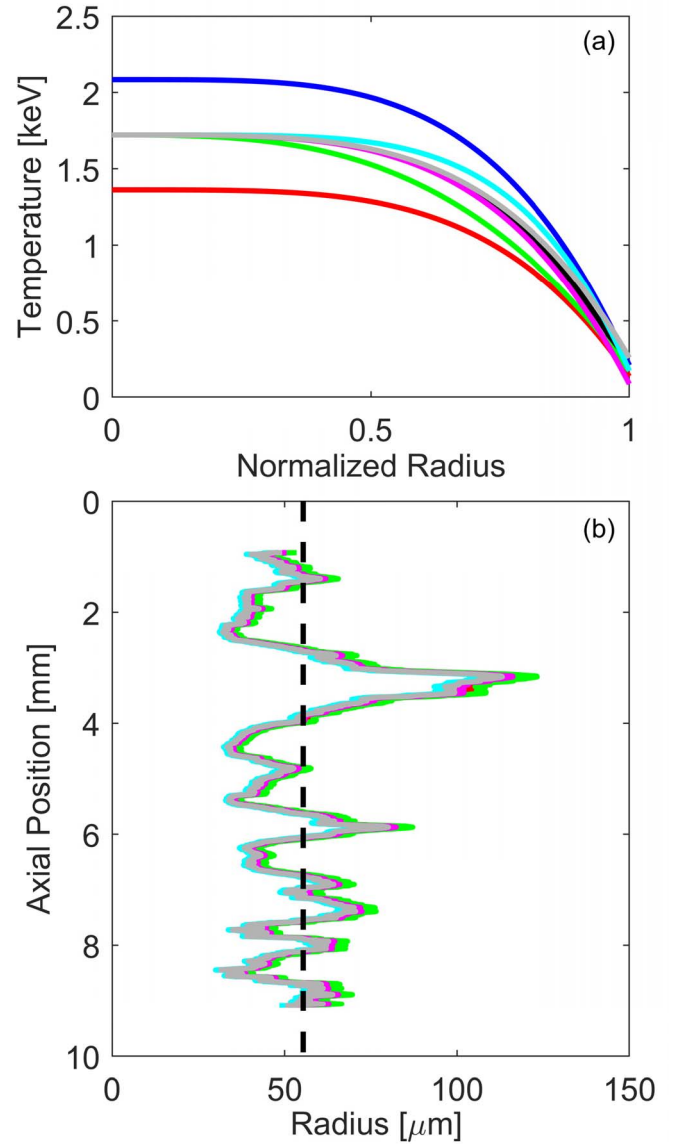


Fig. 8. (a) Plot of several radial temperature profiles that were evaluated to determine the impact of the model assumptions on the inferred radius. Variations included increasing and decreasing T_{peak} to the uncertainty bounds in the ion temperature measurement, increasing and decreasing T_{rad} by 50%, and increasing and decreasing the radial dependence exponent by 1. (b) Plot of the inferred radii with each of the radial temperature profiles for z2707. The different radial temperature profiles changed the inferred radius by less than 10% compared to the nominal profile. The predicted radius for z2707 based on simulations [44] is shown as a dashed vertical line.

analysis with an uncertainty defined by the spread in the values determined with the different radial temperature profile models.

A reconstruction of each experimental image was generated using the inferred radii and intensities from this analysis, as shown in Fig. 9(b). The generated images matched the corresponding experimental images, indicating that the volume estimation was reasonable. However, there were regions where the reconstruction differed from the experimental image. In these regions, the experimental image typically either had multiple peaks or a low-intensity tail. In both cases, these signatures were characteristic of a stagnation column with a

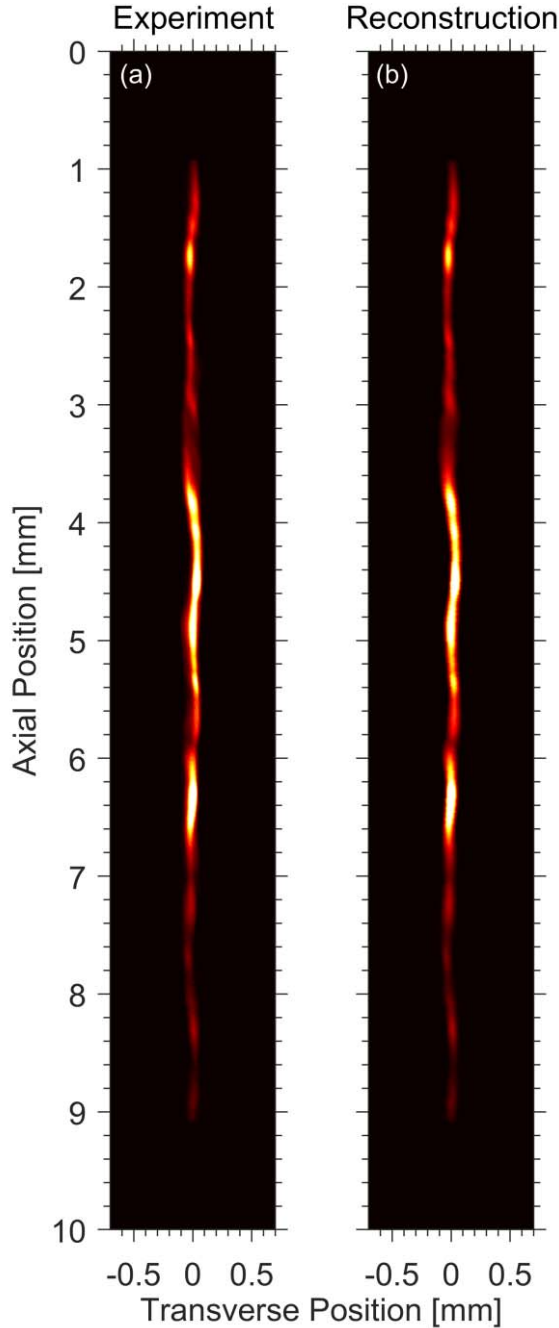


Fig. 9. (a) Experimental self-emission X-ray image from z2707. (b) Reconstructed X-ray image based on the algorithm to determine the fuel radius as a function of axial position.

noncircular cross section; thus, the model was not expected to give a good fit. Fortunately, the model overestimates the volume in regions with multiple peaks and underestimates the volume in regions with a low tail; thus, these effects canceled to some extent.

The burn duration and X-ray yield were estimated using a combination of up to six filtered PCDs and silicon diodes [41]. The diodes were sensitive to X-ray emission in the 1-30 keV range. All channels recorded a narrow peak of emission from the fuel at stagnation, and the lighter filtered channels also

recorded some contribution from the exterior of the liner a few ns later. When necessary, a curve was fit to the liner emission, and it was subtracted to isolate the emission from the fuel. A Gaussian curve was fit to the fuel emission peak, and the full-width at half-maximum was used to approximate the burn duration after accounting for the time response of the diode, which was small compared to the signal width [42], [43]. There was no obvious trend in emission duration with spectral band, so the emission widths were averaged to determine the burn duration, and the spread in widths was used as the uncertainty in the measurement. The X-ray yield in each spectral band was determined by integrating the measured X-ray power radiated by the fuel and accounting for the solid angle of the detector.

At the time of these experiments, the Z Facility did not have a diagnostic to measure burn duration directly from neutron emission. Magnetohydrodynamics simulations indicated that X-ray emission duration was a good surrogate for neutron emission duration [44]. These simulations neglected the impacts of 3-D effects and mix, which were both expected to truncate the neutron emission relative to X-ray emission. Thus, the X-ray emission duration was likely an upper bound on the neutron emission duration.

Using the values for neutron yield, ion temperature, hot fuel volume, burn duration, and X-ray yield, the fuel pressure and mix fraction were estimated assuming a steady-state, isobaric plasma with a circular cross section and a temperature distribution described by (8) [45]. The expected neutron emission from this hot spot was calculated with

$$Y_{DD} = \frac{1}{2} P_{HS}^2 \tau_{burn} \int_V \frac{\langle \sigma v \rangle_{DD}}{(1 + \langle Z \rangle)^2 T(r)^2} dV \quad (13)$$

where V is the plasma volume, $\langle \sigma v \rangle_{DD}$ is the DD fusion reactivity, and $\langle Z \rangle$ is the average charge state of the fuel [45]. Similarly, the X-ray emission was calculated by integrating (9) over the fuel volume. The calculated X-ray spectrum was attenuated by a 0.75-g/cm²-cold beryllium opacity (representing the liner) [39], the spectral sensitivity of each X-ray yield diagnostic (transmission of the filter and absorption of the diode) was applied to the spectrum, and the signal was integrated over energy space to determine the X-ray yield for each spectral band.

The pressure and mix fraction were determined by finding the solution that exactly matched the neutron yield and minimized the least squares difference between the calculated and measured X-ray yields. Note that for this analysis, the mix material was assumed to be fully ionized beryllium, which allowed the beryllium-equivalent mix fraction to be determined. While the mix was likely dominated by other materials in some experiments, determining the mix in beryllium-equivalence allowed for easy comparison of the impact of mix across different types of experiments. A Monte Carlo technique was used to sample the distribution of the measured stagnation parameters, and for each case, the optimal pressure and mix were found.

As shown in Fig. 10, both the pressure and mix distributions had a skew, despite Gaussian distributions for each of the parameters used to determine them. The skew in the pressure

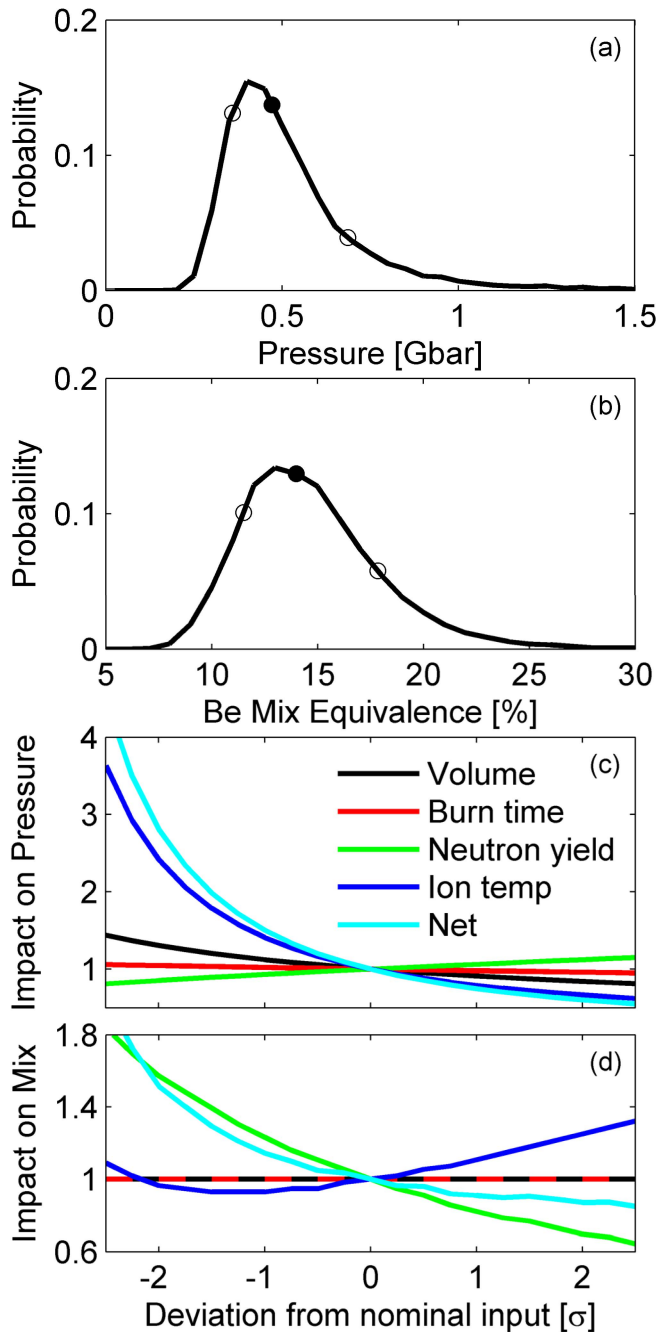


Fig. 10. (a) and (b) Plots of the pressure and beryllium mix equivalence probability distribution functions for z2707. Solid circles indicate the value assuming nominal conditions. Open circles indicate the edges of the central 68.3% of each distribution. (c) and (d) Plots of the correlation between volume, burn duration, neutron yield, and ion temperature and the inferred pressure and mix. The net impact of the input parameter distributions is also included. The ion temperature dominates the skew in the pressure distribution, and the neutron yield dominates the skew in the mix distribution.

distribution was expected primarily due to the nonlinear dependence of the fusion reaction cross section on ion temperature. Similarly, the skew in the mix percentage distribution was primarily due to the different dependence of neutron and X-ray yield on the plasma pressure. The nominal neutron yield, ion temperature, fuel volume, and burn duration were used to

determine the most likely solution for both pressure and mix. The uncertainty was set by the range of values containing the central 68.3% of solutions when the distributions of the input parameters were included.

IV. APPLICATION TO EXPERIMENTS

The experiments included in this analysis were grouped into categories based on the initial fuel density, the height of the target, the cushion [13] material [see Fig. 1(b)], and the approximate laser energy coupled to the fuel. A total of seven configurations were tested, leading to a wide range of stagnation performances. Important trends in performance were identified by comparing between experiment types.

A. Impact of Fuel Density With Low Laser Energy Coupling

Simulations predicted that the first MagLIF experiments could produce more than 10^{13} primary DD neutrons under the assumption that nearly 2 kJ of laser energy was delivered to the fuel [19]. According to the analysis technique described in Section II, these first MagLIF experiments, which used nominally 3.5- μm -thick LEH windows, only coupled 0.4–0.5 kJ of laser energy to the fuel. The difference between simulation and experiment can be accounted for in three major areas. First, the efficiency of the optical chain between the laser energy measurement and the target was overlooked, and it reduced the total energy of the laser pulse from nominally 2.5 kJ to about 2.1 kJ. Second, SBS backscatter, which was not accounted for in the MHD simulations, further reduced the beam energy to about 1.5 kJ. Finally, in early simulations, the window was assumed to deform into a hemisphere, which would reduce the thickness to 50% of the initial value, or 1.75 μm , but measurements showed that the window thickness was only reduced to approximately 3 μm . The attenuation of the thicker than expected window reduced the laser energy to 0.4–0.5 kJ.

With only a few hundred joules of laser energy, postexperiment LASNEX [46] simulations indicated a significant drop in neutron yield for targets with 0.7 kg/m^3 , as shown in Fig. 11. In addition, the calculated neutron yield with 1.4- kg/m^3 fuel was an order of magnitude below the lower density target with very low energy coupling. Note that similar results have been observed previously [19], [25]. As shown in Table II, several experiments were conducted with 0.7- kg/m^3 D_2 gas, and a single experiment was conducted with 1.4- kg/m^3 D_2 gas. Qualitatively, the experimental results followed expectations that in the low coupling limit, the neutron yield for the higher density should be lower. However, the yield degradation for the target with high-density fuel was significantly larger than expected. This could be an indication that the laser energy coupling estimate for the higher density fuel was less accurate. Still, the results were consistent with the hypothesis that the combination of increased fuel density and low laser energy led to the low neutron yield in z2583.

Interestingly, 1-D and 2-D MagLIF simulations indicate that increasing the fuel density will not enable the target to produce a substantially higher neutron yield [25], [44]. Moreover, to reach the same neutron yield, the laser energy coupled needs to scale up roughly proportionally to the fuel

TABLE II
STAGNATION CONDITIONS

Shot	z2583	z2591	z2613	z2707	z2708	z2758	z2768	z2769	z2839	z2850	z2851	z2852	z2985
Fuel Density [kg/m ³]	1.4	0.7	0.7	0.7	0.7	0.7	0.7	0.7	0.7	0.7	0.7	0.7	0.7
Energy delivered to fuel [kJ]	0.48 (+0.27) (-0.31)	0.50 (+0.17) (-0.26)	0.40 (+0.12) (-0.28)	0.87 (+0.26) (-0.24)	1.12 (+0.33) (-0.31)	0.97 (+0.24) (-0.27)	1.20 (+0.36) (-0.32)	1.88 (+0.60) (-0.49)	1.38 (+0.28) (-0.40)	0.52 (+0.16) (-0.32)	0.46 (+0.15) (-0.29)	0.51 (+0.15) (-0.32)	1.02 (+0.30) (-0.28)
Target height [mm]	7.5	7.5	7.5	10	10	10	10	10	10	7.5	10	7.5	10
Cushion material top/bottom	Al/CH	Al/CH	Al/CH	Al/Al	Al/Al	Al/Al	Al/Al	Al/Al	Be/Be	Be/Be	Be/Be	Al/Be	Al/Al
Neutron yield [10 ⁹]	4.5	2000	1100	260	170	310	16	110	3200	3100	1000	2000	180
Ion temp. [keV]	---	2.6	2.0	1.5	1.3	1.6	---	1.2	2.5	2.8	1.8	2.5	1.4
Hot fuel volume [mm ³]	---	---	0.108 ±0.017	0.082 ±0.017	0.113 ±0.019	0.088 ±0.014	0.048 ±0.014	0.106 ±0.022	0.137 ±0.019	0.106 ±0.017	0.105 ±0.017	0.096 ±0.016	0.116 ±0.022
Convergence ratio	---	---	31.9 ±2.6	41.2 ±4.4	35.2 ±3.1	35.5 ±2.8	32.3 ±5.0	34.9 ±3.7	32.4 ±2.3	31.4 ±2.6	36.5 ±3.0	32.4 ±2.7	32.7 ±3.1
Burn duration [ns]	---	1.81 ±0.31	1.38 ±0.15	1.65 ±0.07	1.47 ±0.11	1.49 ±0.04	1.43 ±0.29	1.60 ±0.08	1.76 ±0.22	1.62 ±0.23	1.95 ±0.14	1.67 ±0.22	1.66 ±0.26
Stagnation time relative to 5 MA [ns]	---	96.3	94.4	98.6	98.5	98.6	97.3	98.8	101.0	96.4	104.0	97.8	100.6
Laser relative to stagnation timing [ns]	---	-52.8	-53.8	-55.2	-51.6	-43.5	-33.8	-55.9	-57.2	-52.8	-60.7	-55.3	-58.8
Stagnation pressure [Gbar]	---	---	0.56 (+0.21) (-0.12)	0.47 (+0.22) (-0.11)	0.48 (+0.23) (-0.12)	0.52 (+0.22) (-0.11)	---	0.46 (+0.24) (-0.13)	0.58 (+0.18) (-0.11)	0.60 (+0.18) (-0.11)	0.53 (+0.22) (-0.11)	0.59 (+0.19) (-0.10)	0.37 (+0.19) (-0.10)
Be mix equivalence [%]	---	---	5.0 (+2.7) (-1.8)	14.0 (+3.9) (-2.5)	23.2 (+5.2) (-3.1)	22.0 (+5.2) (-3.4)	---	28.5 (+6.4) (-3.4)	5.0 (+2.8) (-2.2)	5.2 (+2.8) (-2.4)	6.8 (+2.9) (-1.8)	9.0 (+3.2) (-3.0)	14.8 (+4.0) (-2.5)

The stagnation parameters are given along with several input parameters to categorize the experiments. The uncertainties in the neutron yield and ion temperature were $\pm 20\%$. The minimum threshold for the neutron yield measurements was 3×10^9 due to gamma-ray background. All targets had an inner diameter of 4.65 mm and an outer diameter of 5.58 mm. The effective convergence ratio was determined by taking the ratio of the initial fuel radius to the effective stagnation fuel radius. The fuel radius was calculated using $r_f = \sqrt{V/(\pi * h)}$, where V was the stagnation volume and h was the axial extent of the stagnation emission. The uncertainties in the convergence ratios were determined by assuming the volume was $\pm 1\sigma$ and repeating the calculation. The uncertainties in the relative times were ± 1.4 ns based on a ± 1 ns absolute uncertainty in each Z Facility diagnostic.

density (effectively conserving fuel temperature at the time of laser heating) [25], [44]. The main advantage of increasing the fuel density is a reduced convergence ratio at stagnation, which would increase confidence in predictions of target performance and scaling. In addition, with reduced convergence, nonideal behaviors, such as 3-D effects and mix, should have a smaller impact, which could improve target performance.

B. Laser Energy Effect on Mix Fraction

As shown in Table II, subsequent experiments with nominally 1.8- μm -thick windows did couple more energy than experiments with 3.5- μm -thick windows. At 0.8–1.2 kJ, the energy coupled in these experiments was near optimal for

these targets according to 2-D simulations without mix [44]. Thus, the observed decrease in neutron yield and ion temperature relative to previous experiments was unexpected at the time. The degradation in performance can be explained by the substantial increase in the inferred beryllium-equivalent mix fraction. Compared to the experiments with thicker windows and lower laser energy, the inferred mix increased by an average of 2.6x.

Within this class of target (1.8- μm -thick window, 10-mm tall, aluminum cushions), the laser energy coupled to the fuel was increased by increasing the laser power (z2708/z2985) or increasing the duration of the laser (z2769). As shown in Fig. 12, the neutron yield and ion temperature decreased with increasing laser energy. The inferred mix in these

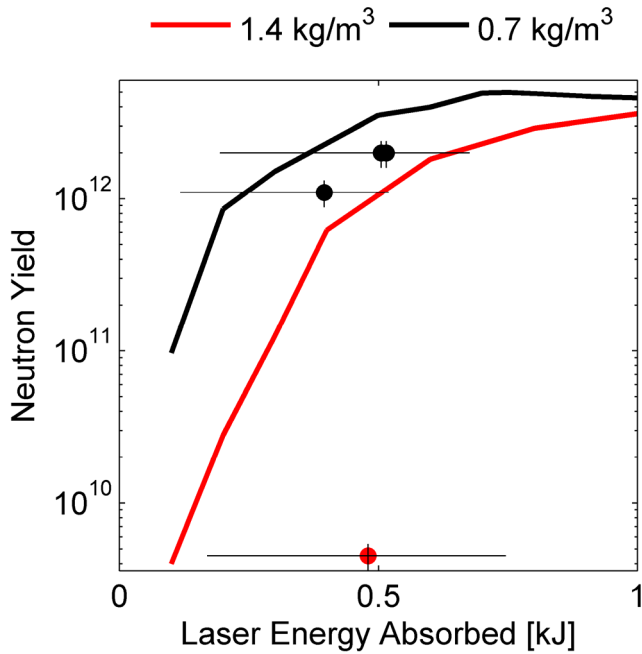


Fig. 11. Plot of the experimental yield as a function of the coupled laser energy for 7.5-mm targets with 0.7- and 1.4-kg/m³ initial fuel densities. Curves from LASNEX simulations [44] of the same target types are overlaid for comparison to show that performance was expected to degrade significantly with low coupled laser energy, especially at the higher initial fuel density.

experiments increased with increasing laser energy, indicating that even lower laser coupling may have been optimal for these targets.

A series of LASNEX simulations were conducted to demonstrate that the optimal laser energy decreased in targets when mix was assumed to be correlated with coupled laser energy, as shown in Fig. 13. In these simulations, the mix fraction was assumed to scale linearly with the laser energy coupled to the fuel, and the mix was instantaneously, uniformly distributed throughout the fuel. These simulations were not intended to model the experiments with aluminum cushions from Fig. 12, rather they were meant to qualitatively show that in experiments where mix increases with increasing laser energy coupled, the optimal laser energy shifts to a lower value, and the maximum achievable yield is reduced. The simulations are qualitatively consistent with the observed experimental reduction in neutron yield and increase in mix with increased laser energy coupled to the fuel.

The inferred mix in these targets was calculated in terms of beryllium equivalence, but it was likely composed of several different materials from several sources [30], [45]. LEH window material (polyimide), top cushion/LEH channel material (aluminum), and bottom cushion material (aluminum) could all be injected around the time of laser heating. Liner wall material (beryllium) is likely injected primarily during the deceleration stage just before stagnation, approximately 50-ns later.

In a subsequent experiment (z2839), the cushion material was changed from aluminum to beryllium with the intent

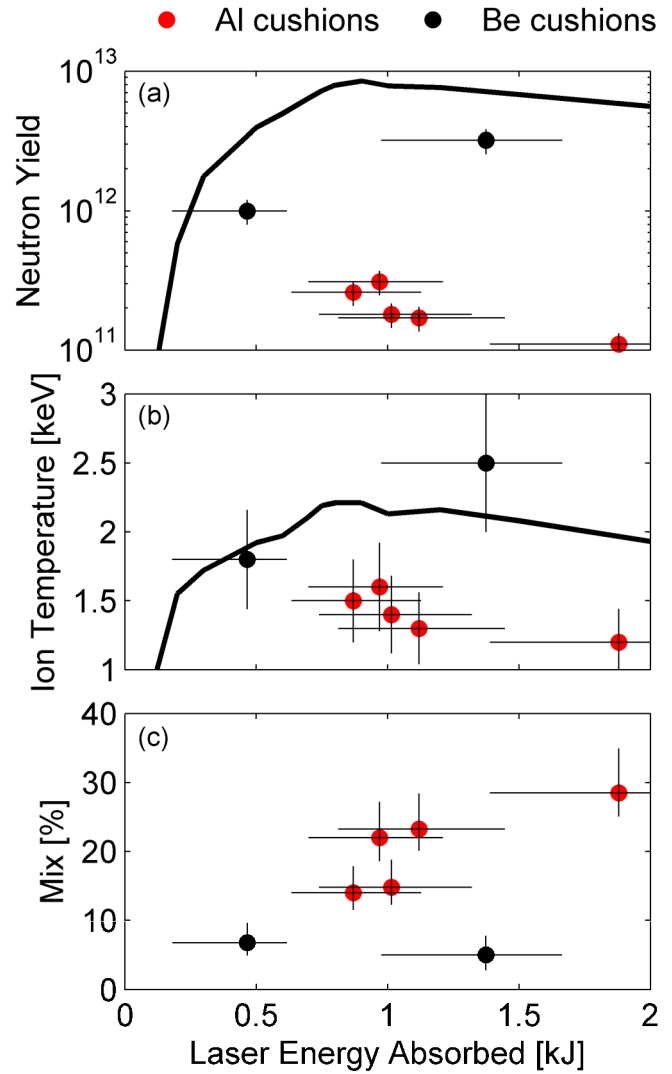


Fig. 12. (a)–(c) Plots of the neutron yield, ion temperature, and inferred mix as a function of the coupled laser energy for the 10-mm targets with aluminum and beryllium cushions. Solid lines in (a) and (b) represent LASNEX simulation results [44], and red and black circles indicate the experimental results for targets with aluminum and beryllium cushions, respectively. Experiments with beryllium cushions produced around 40% of the neutron yield predicted in simulations, whereas targets with aluminum cushions only produced 2%–4% of the predicted yields. Significantly increased mix was observed for the targets with aluminum cushions, explaining the low yields and ion temperatures.

of reducing the impact of mix from the cushion. Cushion mix was targeted for several reasons. The inferred mix had a dependence on laser energy coupling, indicating a main source of mix likely occurred at the time of laser heating, and simulations indicated that mix at the time of laser heating was far more detrimental than mix just prior to stagnation [44]. In addition, in these experiments, the top and bottom cushions were aluminum, which would produce a proportionally greater contribution to the inferred mix due to the higher atomic number compared to polyimide and beryllium (proportional to Z^3) [45].

Replacing the aluminum cushions with beryllium cushions led to an order of magnitude increase in neutron yield, over a

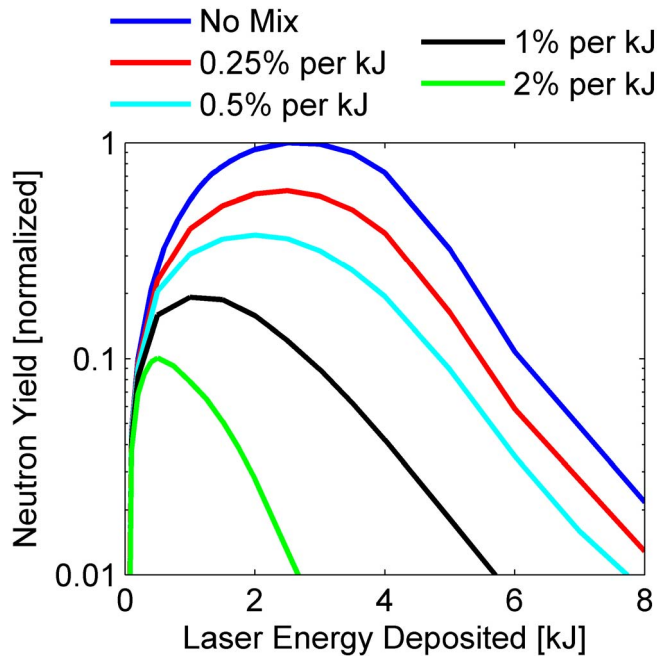


Fig. 13. Plot of simulated neutron yields as a function of laser energy without mix and for several cases where the beryllium mix fraction was linearly dependent on the laser energy coupled. For the cases with greater mix fraction per laser energy deposition, the optimal laser energy was lower, and the maximum possible neutron yield was reduced.

50% increase in ion temperature, and a factor of 4 reduction in inferred beryllium mix equivalence [45]. Interestingly, the mix fraction may not have changed or possibly even increased, but the lower atomic number of the mix material reduced the beryllium mix equivalence [45] and the impact that mix had on stagnation performance. With the reduced impact of mix, the experimental neutron yield was within a factor of 2.5 of the expected yield from 2-D simulations without mix, as shown in Fig. 12(a).

The impact of cushion material on target performance with low laser energy coupled to the fuel was also assessed. Beryllium cushions were used in an experiment (z2850) with a nominally 3.5- μm -thick LEH window, which limited the laser energy coupled to the fuel to approximately 0.52 kJ. The neutron yield increased and the inferred beryllium mix equivalence decreased compared to the average values for experiments with an aluminum top cushion (z2591/z2613/z2852); however, the effects were small compared to the case with high laser energy coupling.

The inferred beryllium mix equivalence as a function of laser energy coupled to the fuel was plotted in Fig. 12(c). Based on this series of experiments, mix from the cushions negatively impacted the target performance, and the importance of this mix increased with increasing laser energy. Unfortunately, it could not be determined if the source of the mix was the top cushion, the bottom cushion, or both. The energy deposited by the laser was greatest at the top of the target, which should have resulted in greater radiative ablation of the top cushion by the laser heated fuel and a stronger blast wave interacting with the ablated material, mixing it

into the fuel. Conversely, the laser could have filamented and directly struck the face of the bottom cushion, ablating material into the fuel. Both effects were expected to increase with laser energy. Additional experiments focused on diagnosing cushion mix hint that both top and bottom cushion mix may be important [30].

C. Scaling With Laser Energy in Low-Mix Limit

Two experiments (z2839/z2851) were conducted with nominally identical configurations aside from a difference in the LEH window thickness, which produced a difference in laser energy coupled to the fuel. Both experiments used beryllium cushions to limit the deleterious impact of mix on the stagnation performance. Increasing the laser energy coupled from 0.46 to 1.38 kJ resulted in over a factor of 3 increase in neutron yield and more than a 30% increase in ion temperature. The trends are consistent with those observed in the 2-D MHD simulations without mix.

With increased laser energy coupled to the fuel, the effective convergence ratio at stagnation decreased from 36 to 32. In 1-D or 2-D, the convergence is determined by when the fuel pressure is sufficient to stop the liner implosion. In both experiments, the current driving the implosion was nominally the same, but the internal energy of the fuel was higher in the experiment with increased laser energy coupled to the fuel. This should result in stagnation at a larger radius, as was observed experimentally.

The inferred beryllium mix equivalence decreased slightly with increased laser energy. For these experiments, the change in laser energy coupled to the fuel was the result of the change in the LEH window thickness. Assuming that the window material mix was roughly proportional to the window mass in the laser path, the experiment with lower laser energy coupling would have roughly twice the window mix. In the thin window case, window material accounted for 1.5%–2% of the beryllium mix equivalence [45]; doubling this would nearly account for the difference between the two experiments. The increased convergence in the experiment with low laser energy coupling should also exacerbate deceleration mix from the liner. These two increases in mix could more than makeup for the anticipated decrease in cushion mix with decreased laser energy coupled to the fuel.

D. Impact of Target Height

The height of the target impacts the inductance of the load, which affects the current delivery to the target; taller targets have higher inductance. The increase in inductance places a higher voltage stress on the posthole convolute and transmission lines [47], which results in increased current loss. Moreover, even in a lossless system, the load current would decrease with increased inductance, assuming a fixed driving voltage pulse.

B-dot current monitors located at a radius of 5.9 cm typically have been used to determine the load current at the Z Facility. The inductance inside the convolute was very high for the MagLIF experiments; thus, large current losses were expected. The B-dot monitors have not performed well

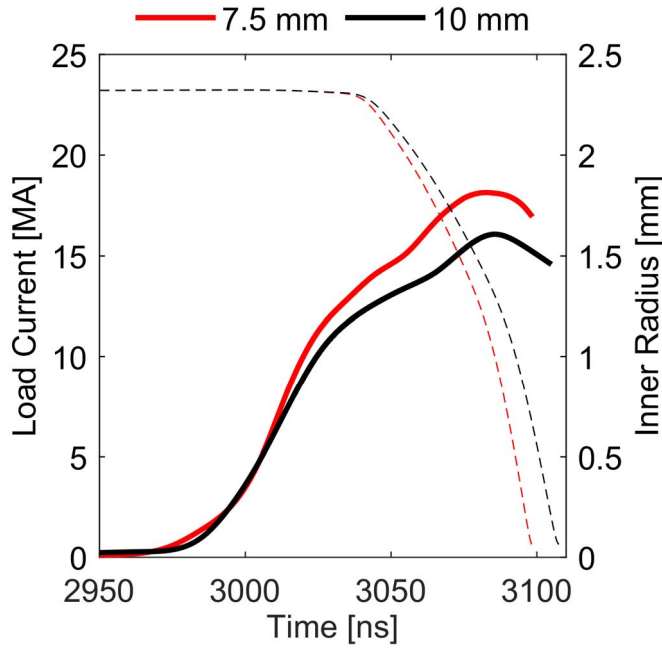


Fig. 14. Plot of the currents inferred from velocimetry at the load for 7.5- (z2850) and 10-mm (z2851) targets (thick solid lines) and the simulated [40] liner inner radius trajectories (thin dashed lines). The increased inductance of the 10-mm target resulted in approximately 2-MA lower peak load current.

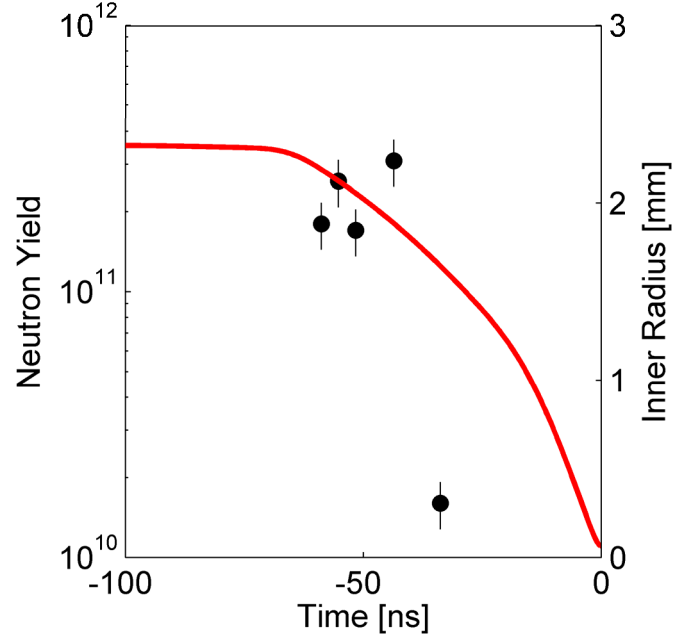


Fig. 15. Plot of the neutron yield as a function of laser heating time relative to stagnation (black dots) and the simulated liner inner radius trajectory (red line). The targets performed nominally when laser heating occurred between 43 and 59 ns prior to stagnation but performed poorly when laser heating occurred 34 ns prior to stagnation, at which time the liner radius was similar to the size of the LEH radius (1.5 mm).

on experiments with high losses [47] and have not accurately reflected the current at the load in the MagLIF experiments. Velocimetry of a current-carrying surface at the load [48] was used to accurately determine the load current [49], [50] for both a 7.5-mm target and a 10-mm target, as shown in Fig. 14. The peak load current for the 7.5-mm target was 18.1 MA compared to 16.1 MA for the 10-mm target. The impact of the change in load current was observed in the implosion times of the two target types. The average time between when the stack current reached 5 MA and stagnation was 96.2 ± 1.4 ns for 7.5-mm targets and 99.7 ± 2.1 ns for 10-mm targets.

The target height also impacts the laser heating stage of MagLIF. In the limit of low laser energy, a longer target results in a fixed energy shared by a larger fuel mass, which produces a lower preheat temperature. In the high-energy limit, the laser penetrates deeper into the target; thus, a longer target could limit the energy reaching the bottom cushion, which could reduce mix. The longer targets also reduce axial fuel loss during the implosion [19].

Two experiments (z2850/z2851) were conducted with nominally identical configurations other than a difference in load height. The experiments were operated in the low laser energy limit with beryllium cushions to reduce the impact of mix. The 7.5-mm target produced 3.1x higher neutron yield and a 50% increase in ion temperature compared to the 10-mm target. The 7.5-mm target was expected to perform better due to both the increased current and the increased preheat temperature of the fuel. To isolate these effects, a simulation of the 7.5-mm target with 0.52 kJ of laser energy coupled was compared with a 7.5-mm target with 0.34 kJ coupled

(equivalent to the energy-to-fuel mass ratio in the 10-mm target). The simulations predicted 1.9x higher yield with the increase in laser energy coupled. This implies that the increased current accounted for approximately 1.6x higher yield; thus, the neutron yield approximately scaled as current to the fourth power.

While this is roughly the expected scaling with current, it is important to note that this is only based on two experimental data points, the difference between the peak current for these cases is small, there are uncertainties in the neutron yield and load current measurements, and idealized 2-D simulations were used to account for the difference in laser heating due to target height. This result suggests that yield scales roughly as current to the fourth power, but it should not be used to extrapolate the expected performance at higher currents. Additional experiments with peak load currents that span from approximately 12 to 22 MA are planned to solidify current scaling arguments.

On average, the stagnation pressure in experiments with 7.5-mm targets was 1.2x higher than the stagnation pressure in experiments with 10-mm targets, which was expected due to the increased current (and drive pressure) in the experiments with 7.5-mm targets. The observed trend was roughly consistent with the ratio of stagnation pressures in the 2-D MHD simulations of the two target heights [44]. However, the experiments with the highest pressures were also the ones with the lowest inferred mix and fuel convergence ratios; thus, the increase in stagnation pressure was not definitively caused by the increase in load current.

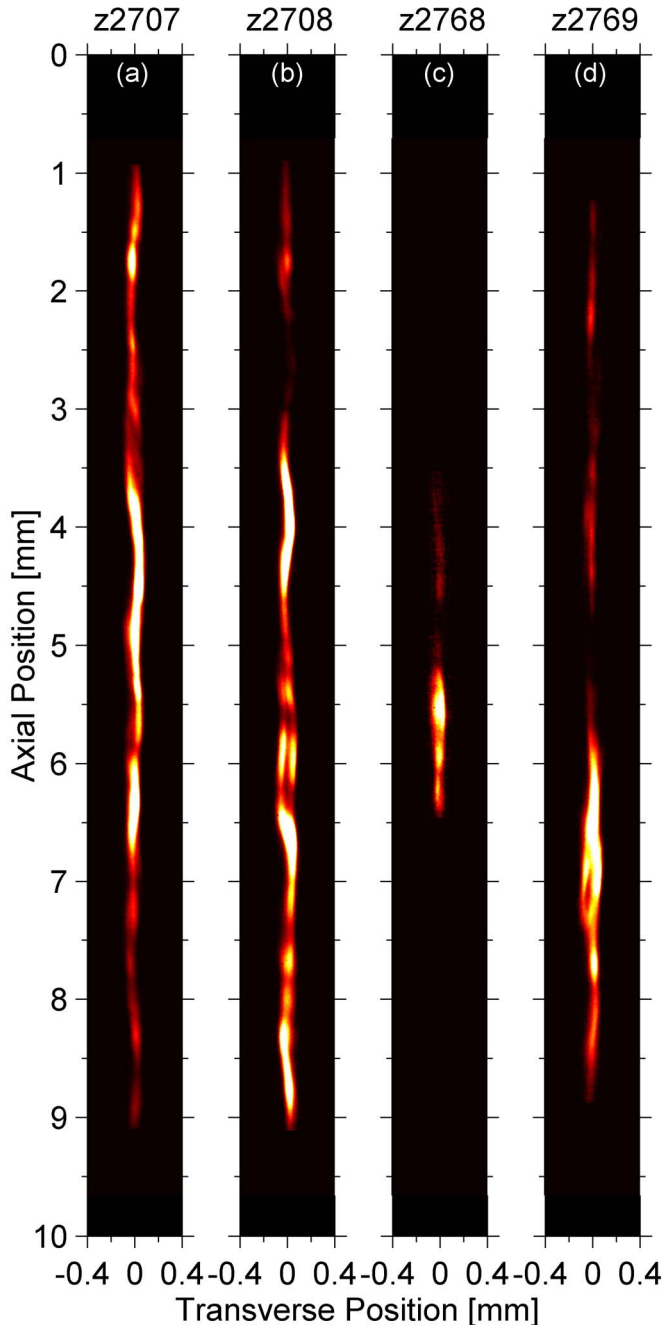


Fig. 16. (a)–(d) X-ray self-emission images for four experiments with 10-mm targets and aluminum cushions with a variety of laser configurations. The laser was fired late in z2768, resulting in a significantly reduced axial emission height. The laser energy was increased by about a factor of two in z2769, resulting in a significant difference in emission intensity and radius over the axial extent. Note that a fiducial blocked the signal at roughly 5 mm from the top of the target in z2768 and z2769.

E. Effect of Laser Timing

Based on 2-D MHD simulations without mix, the optimal time to laser heat the fuel should be about 60 ns prior to stagnation [11], [19], when the inner surface of the liner begins to move, thus maximizing the potential PdV work that the liner could do on the fuel while minimizing the time

for radiative losses. The predicted yield decreases slowly as the laser heating stage is moved closer to stagnation, but the convergence also increases [19], which increases uncertainty in the predicted trend. In most MagLIF experiments, the laser heating stage occurs between 52 and 60 ns prior to stagnation.

The time between laser heating and stagnation was varied in a series of experiments with 10-mm targets with aluminum cushions and 1.8- μm -thick LEH windows. Based on these experiments, there was relatively flat performance over a wide range of laser timing; however, for very late times, there was a significant decrease in neutron yield, as shown in Fig. 15. At the time of laser heating in the experiment with reduced neutron yield, the inner surface of the liner was at a radius of 1.6 mm according to a 1-D model of the implosion [40].

The stagnation column images for three of the experiments that evaluated the impact of laser timing are compared in Fig. 16(a)–(c). Interestingly, the stagnation columns in each of these experiments had very similar effective convergence ratios, but the axial extent of the plasma was significantly truncated in the experiment where laser heating occurred approximately 30 ns prior to stagnation. The reduced axial extent of stagnation emission could have been produced by the laser filamenting and striking the liner wall, resulting in significantly increased mix during the preheat stage. In experiments where the laser heating occurred at earlier times, there was more room for the beam within the fuel volume; thus, the laser was less likely to strike the wall of the target.

V. CONCLUSION

Following the initial MagLIF experiments, the lower than expected neutron yield was explained with the hypothesis that the laser energy coupled to the fuel was much lower than the expected [19], [25]. According to the analysis in Section II, the laser energy coupled to the fuel in the first experiments was significantly less than the roughly 2 kJ that was initially expected. Assuming the 0.4–0.5 kJ of laser energy coupled suggested by this analysis, the experimental neutron yields were only about a factor of 2 lower than in simulations [44]. The additional performance degradation was likely due to mix and/or 3-D structure.

In subsequent experiments with nominally 1.5- μm -thick LEH windows, the laser energy deposition was nearly optimal according to 2-D simulations without mix [44]. Targets with mid-Z fuel-facing components performed poorly, while targets with only low-Z-facing components performed close to optimality [45]. The inferred mix increased with laser energy in targets with mid-Z fuel-facing components, indicating that the mix was introduced during the laser heating stage, which was significantly more detrimental than if the mix had been introduced during the liner deceleration stage [44]. In experiments with low mix, neutron yield and ion temperature increased with laser energy, and effective convergence ratio decreased with laser energy, all scaling are approximately as expected.

The target height was increased from 7.5 to 10 mm during this series of experiments. The increased load inductance of the taller target resulted in lower current and reduced ion temperature and neutron yield in the low preheat limit. However, the increase in height combined with thinner windows

enabled more laser energy to be coupled to the fuel without an increase in the inferred mix. The combination of the reduced current and increased preheat nearly canceled one another; the changes in neutron yield and ion temperature were within the uncertainty in the measurements. As a result, the target height in the future experiments could be chosen to favor laser heating or load current, depending on the objective of the experiment.

The time of laser heating relative to stagnation did not have a significant impact on target performance over a wide range. When the laser heating occurred very late, the laser may have directly struck the liner, resulting in significantly reduced neutron yield and increased mix. The cross timing between the Z-Beamlet laser and the Z machine can be set to within approximately ± 3 ns; thus, the laser heating stage can be executed reliably during the window where nominal performance was observed.

The methodologies to assess laser energy deposition and stagnation pressure and mix were useful in establishing trends across a variety of experiments. The simplicity and speed of these techniques allowed evaluation of a large data set; however, these bulk parameter estimates did not account for more nuanced effects. There were significant axial modulations in the X-ray emission images, as shown in Fig. 16(d), which implies variations in the fuel conditions existed, but they could not be accounted for in this analysis because the other diagnostic signals were spatially integrated. Efforts to develop spatially resolved stagnation parameter estimates, which require recently developed diagnostics that were not available for these early MagLIF experiments, are underway.

ACKNOWLEDGMENT

The authors would like to thank Z Facility and Z-Beamlet operations and target fabrication for their contributions to this paper. This paper describes the objective technical results and analysis. Any subjective views or opinions that might be expressed in this paper do not necessarily represent the views of the U.S. Department of Energy or the U.S. Government.

REFERENCES

- [1] M. Shimada *et al.*, "ITER physics basis," *Nucl. Fusion*, vol. 47, no. 6, p. S1, 2007, doi: [10.1088/0029-5515/47/6/S01](#).
- [2] R. J. Hawryluk, "Results from deuterium-tritium tokamak confinement experiments," *Rev. Mod. Phys.*, vol. 70, no. 2, pp. 537–587, 1998, doi: [10.1103/RevModPhys.70.537](#).
- [3] R. C. Wolf *et al.*, "Wendelstein 7-X program—Demonstration of a stellarator option for fusion energy," *IEEE Trans. Plasma Sci.*, vol. 44, no. 9, pp. 1466–1471 Sep. 2016, doi: [10.1109/TPS.2016.2564919](#).
- [4] J. Lindl, "Development of the indirect-drive approach to inertial confinement fusion and the target physics basis for ignition and gain," *Phys. Plasmas*, vol. 2, no. 11, p. 3933, 1995, doi: [10.1063/1.871025](#).
- [5] R. Betti *et al.*, "Thermonuclear ignition in inertial confinement fusion and comparison with magnetic confinement," *Phys. Plasmas*, vol. 17, no. 5, p. 058102 2010, doi: [10.1063/1.3380857](#).
- [6] O. A. Hurricane *et al.*, "Fuel gain exceeding unity in an inertially confined fusion implosion," *Nature*, vol. 506, pp. 343–348, Feb. 2014, doi: [10.1038/nature13008](#).
- [7] I. R. Lindemuth and R. C. Kirkpatrick, "Parameter space for magnetized fuel targets in inertial confinement fusion," *Nucl. Fusion*, vol. 23, no. 3, p. 263, 1983, doi: [10.1088/0029-5515/23/3/001](#).
- [8] M. M. Basko, A. J. Kemp, and J. Meyer-ter-Vehn, "Ignition conditions for magnetized target fusion in cylindrical geometry," *Nucl. Fusion*, vol. 40, no. 1, p. 59, 2000, doi: [10.1088/0029-5515/40/1/305](#).
- [9] J. H. Degnan *et al.*, "Compression of plasma to megabar range using imploding liner," *Phys. Rev. Lett.*, vol. 82, no. 13, pp. 2681–2684, 1999, doi: [10.1103/PhysRevLett.82.2681](#).
- [10] S. C. Hsu and S. J. Langendorf, "Magnetized plasma target for plasma-jet-driven magneto-inertial fusion," *J. Fusion Energy*, vol. 38, no. 1, pp. 182–198, 2019, doi: [10.1007/s10894-018-0168-z](#).
- [11] S. A. Slutz *et al.*, "Pulsed-power-driven cylindrical liner implosions of laser preheated fuel magnetized with an axial field," *Phys. Plasmas*, vol. 17, no. 5, p. 056303, 2010, doi: [10.1063/1.3333505](#).
- [12] M. E. Cuneo *et al.*, "Magnetically driven implosions for inertial confinement fusion at Sandia national laboratories," *IEEE Trans. Plasma Sci.*, vol. 40, no. 12, pp. 3222–3245, Dec. 2012, doi: [10.1109/TPS.2012.2223488](#).
- [13] T. J. Awe *et al.*, "Modified helix-like instability structure on imploding z-pinch liners that are pre-imposed with a uniform axial magnetic field," *Phys. Plasmas*, vol. 21, no. 5, p. 056303, 2014, doi: [10.1063/1.4872331](#).
- [14] D. C. Rovang *et al.*, "Pulsed-coil magnet systems for applying uniform 10–30 T fields to centimeter-scale targets on Sandia's Z facility," *Rev. Sci. Instrum.*, vol. 85, no. 12, p. 124701, 2014, doi: [10.1063/1.4902566](#).
- [15] P. K. Rambo *et al.*, "Z-Beamlet: A multikilojoule, terawatt-class laser system," *Appl. Opt.*, vol. 44, no. 12, pp. 2421–2430, 2005, doi: [10.1364/AO.44.002421](#).
- [16] P. Rambo *et al.*, "Sandia's Z-backlighter laser facility," *Proc. SPIE*, vol. 10014, pp. 100140Z-1–100140Z-16, Dec. 2016, doi: [10.1117/12.2245271](#).
- [17] M. E. Savage *et al.*, "Status of the Z pulsed power driver," in *Proc. 18th IEEE Pulsed Power Conf.*, Chicago, IL, USA, 2011, pp. 983–990, doi: [10.1109/PPC.2011.6191629](#).
- [18] D. V. Rose *et al.*, "Three-dimensional electromagnetic model of the pulsed-power Z-pinch accelerator," *Phys. Rev. Accel. Beams*, vol. 13, p. 010402, Jan. 2010, doi: [10.1103/PhysRevSTAB.13.010402](#).
- [19] A. B. Sefkow *et al.*, "Design of magnetized liner inertial fusion experiments using the Z facility," *Phys. Plasmas*, vol. 21, no. 7, p. 072711, 2014, doi: [10.1063/1.4890298](#).
- [20] M. R. Gomez *et al.*, "Experimental demonstration of fusion-relevant conditions in magnetized liner inertial fusion," *Phys. Rev. Lett.*, vol. 113, p. 155003, Oct. 2014, doi: [10.1103/PhysRevLett.113.155003](#).
- [21] P. F. Schmit *et al.*, "Understanding fuel magnetization and mix using secondary nuclear reactions in magneto-inertial fusion," *Phys. Rev. Lett.*, vol. 113, p. 155004, Oct. 2014, doi: [10.1103/PhysRevLett.113.155004](#).
- [22] P. F. Knapp *et al.*, "Effects of magnetization on fusion product trapping and secondary neutron spectra," *Phys. Plasmas*, vol. 22, no. 5, p. 056312, 2015, doi: [10.1063/1.4920948](#).
- [23] K. D. Hahn *et al.*, "Fusion-neutron measurements for magnetized liner inertial fusion experiments on the Z accelerator," *J. Phys., Conf. Ser.*, vol. 717, no. 1, p. 012020, 2016, doi: [10.1088/1742-6596/717/1/012020](#).
- [24] S. B. Hansen *et al.*, "Diagnosing magnetized liner inertial fusion experiments on Z," *Phys. Plasmas*, vol. 22, no. 5, p. 056313, 2015, doi: [10.1063/1.4921217](#).
- [25] R. D. McBride *et al.*, "Exploring magnetized liner inertial fusion with a semi-analytic model," *Phys. Plasmas*, vol. 23, no. 1, p. 012705, 2016, doi: [10.1063/1.4939479](#).
- [26] M. R. Gomez *et al.*, "Demonstration of thermonuclear conditions in magnetized liner inertial fusion experiments," *Phys. Plasmas*, vol. 22, no. 5, p. 056306, 2015, doi: [10.1063/1.4919394](#).
- [27] M. Geissel *et al.*, "Nonlinear laser-plasma interaction in magnetized liner inertial fusion," *Proc. SPIE*, vol. 9731, pp. 97310-1–97310-7, Mar. 2016, doi: [10.1117/12.2218577](#).
- [28] M. Geissel *et al.*, "Minimizing scatter-losses during pre-heat for magneto-inertial fusion targets," *Phys. Plasmas*, vol. 25, no. 2, p. 022706, 2018, doi: [10.1063/1.5003038](#).
- [29] A. J. Harvey-Thompson *et al.*, "Constraining preheat energy deposition in MagLIF experiments with multi-frame shadowgraphy," *Phys. Plasmas*, to be published.
- [30] A. J. Harvey-Thompson *et al.*, "Diagnosing and mitigating laser preheat induced mix in MagLIF," *Phys. Plasmas*, vol. 25, no. 11, p. 112705, 2018, doi: [10.1063/1.5050931](#).
- [31] W. K. Schomburg, "Membranes," in *Introduction to Microsystem Design*, 1st ed. New York, NY, USA: Springer, 2011, pp. 29–52.
- [32] M. M. Marinak *et al.*, "Three-dimensional HYDRA simulations of National Ignition Facility targets," *Phys. Plasmas*, vol. 8, no. 5, p. 2275, 2001, doi: [10.1063/1.1356740](#).

- [33] T. Goorley, "MCNP6.1.1-beta release notes," Los Alamos Nat. Lab., Los Alamos, NM, USA, Tech. Rep. LA-UR-14-24680, 2014.
- [34] C. L. Ruiz *et al.*, "Production of thermonuclear neutrons from deuterium-filled capsule implosions driven by Z-pinch dynamic hohlraums," *Phys. Rev. Lett.*, vol. 93, p. 015001, Jun. 2004, doi: [10.1103/PhysRevLett.93.015001](#).
- [35] L. Ballabio, J. Källne, and G. Gorini, "Relativistic calculation of fusion product spectra for thermonuclear plasmas," *Nucl. Fusion*, vol. 38, no. 11, pp. 1723–1735, 1998, doi: [10.1088/0029-5515/38/11/310](#).
- [36] R. Hatarik *et al.*, "Analysis of the neutron time-of-flight spectra from inertial confinement fusion experiments," *J. Appl. Phys.*, vol. 118, no. 18, p. 184502, 2015, doi: [10.1063/1.4935455](#).
- [37] H. Brysk, "Fusion neutron energies and spectra," *Plasma Phys.*, vol. 15, no. 7, pp. 611–617, 1973, doi: [10.1088/0032-1028/15/7/001](#).
- [38] E. C. Harding *et al.*, "Single and dual-crystal X-ray microscopes for large field-of-view self-emission imaging on the Z-machine," to be published.
- [39] S. B. Hansen, E. C. Harding, P. F. Knapp, M. R. Gomez, T. Nagayama, and J. E. Bailey, "Fluorescence and absorption spectroscopy for warm dense matter studies and ICF plasma diagnostics," *Phys. Plasmas*, vol. 25, no. 5, p. 056301, 2018, doi: [10.1063/1.5018580](#).
- [40] R. D. McBride and S. A. Slutz, "A semi-analytic model of magnetized liner inertial fusion," *Phys. Plasmas*, vol. 22, no. 5, p. 052708, 2015, doi: [10.1063/1.4918953](#).
- [41] M. C. Jones *et al.*, "X-ray power and yield measurements at the refurbished Z machine," *Rev. Sci. Instrum.*, vol. 85, no. 8, p. 083501, 2014, doi: [10.1063/1.4891316](#).
- [42] D. R. Kania, M. I. Landstrass, M. A. Plano, L. S. Pan, and S. Han, "Diamond radiation detectors," *Diamond Rel. Mater.*, vol. 2, pp. 1012–1019, Apr. 1993, doi: [10.1016/0925-9635\(93\)90266-5](#).
- [43] G. C. Idzorek and R. J. Bartlett, "Silicon photodiode characterization from 1 eV to 10 keV," *Proc. SPIE*, vol. 3114, pp. 349–357, Oct. 1997, doi: [10.1117/12.278897](#).
- [44] S. A. Slutz *et al.*, "Enhancing performance of magnetized liner inertial fusion at the Z facility," *Phys. Plasmas*, vol. 25, no. 11, p. 112706, 2018, doi: [10.1063/1.5054317](#).
- [45] P. F. Knapp *et al.*, "Origins and effects of mix on magnetized liner inertial fusion target performance," *Phys. Plasmas*, vol. 26, no. 1, p. 012704, 2019, doi: [10.1063/1.5064548](#).
- [46] G. B. Zimmerman and W. L. Kruer, "Numerical simulation of laser-initiated fusion," *Comments Plasma Phys. Controlled Fusion*, vol. 2, no. 2, pp. 51–60, 1975.
- [47] M. R. Gomez *et al.*, "Experimental study of current loss and plasma formation in the Z machine post-hole convolute," *Phys. Rev. Accel. Beams*, vol. 20, p. 010401, Jan. 2017, doi: [10.1103/PhysRevAccelBeams.20.010401](#).
- [48] C. A. Hall, "Isentropic compression experiments on the Sandia Z accelerator," *Phys. Plasmas*, vol. 7, no. 5, pp. 2069–2075, 2000, doi: [10.1063/1.874029](#).
- [49] C. A. Jennings *et al.*, "Assessing the current delivered by the Z generator to MagLIF ICF experiments," to be published.
- [50] A. Porwitzky and J. Brown, "Uncertainties in cylindrical anode current inferences on pulsed power drivers," *Phys. Plasmas*, vol. 25, no. 6, p. 063102, 2018, doi: [10.1063/1.5026983](#).



Matthew R. Gomez (M'06) received the B.S.E. and M.S.E. degrees in nuclear engineering and radiological sciences, the M.S.E. degree in electrical engineering and computer science, and the Ph.D. degree in nuclear engineering and radiological sciences from the University of Michigan at Ann Arbor, Ann Arbor, MI, USA, in 2005, 2007, 2008, and 2011, respectively.

Since 2011, he has been a Staff Member with Sandia National Laboratories, Albuquerque, NM, USA where he studies inertial confinement fusion and high-energy density science on the Z machine. His current research interests include magneto-inertial fusion sources, power flow and current coupling in large pulsed power drivers, and X-ray diagnostic development.



Stephen A. Slutz received the Ph.D. degree in astrophysics from the California Institute of Technology, Pasadena, CA, USA, in 1978.

Since 1978, he has been with Sandia National Laboratories, Albuquerque, NM, USA, where he is currently a Distinguished Member of Technical Staff. At Sandia, he designed the light ion-driven inertial fusion targets, including the greenhouse target, which was adopted as the main approach to light ion fusion. He also developed magnetically insulated light ion diodes both theoretically and experimentally, for which he holds a patent. He was the Chief Theorist of the Z-pinch driven dynamic hohlraums, designing and simulating dynamic hohlraums to drive inertial fusion targets, which held the record neutron yield for the pulsed power driven fusion in 2006. His contributions to the magnetized liner inertial fusion concept include demonstrating numerically that high gain is possible with the magneto-inertial fusion and the development of automagnetizing liner to obtain highly magnetized fuel.

Dr. Slutz is a fellow of the American Physical Society. He received the 2004 Lockheed Martin Nova Award for his work on Z-pinch driven dynamic hohlraums.



Patrick F. Knapp received the Ph.D. degree in electrical and computer engineering from Cornell University, Ithaca, NY, USA, in 2011.

He then joined the Staff at Sandia National Laboratories, Albuquerque, NM, USA. As a Researcher with the Center for Pulsed Power Sciences, Sandia National Laboratories, he conducts experiments on the 20-MA Z machine to investigate inertial confinement fusion and high-energy density plasma physics.



Kelly D. Hahn (M'08) received the B.S.E.E., M.S.E.E., and Ph.D. degrees in electrical engineering from The University of New Mexico, Albuquerque, NM, USA, in 1999, 2002, and 2006, respectively.

From 2001 to 2010, she was with Sandia National Laboratories, Albuquerque, NM, USA, where she was developing intense electron-beam-driven flash X-ray radiography sources. From 2010 to 2018, she was involved in nuclear measurements for inertial confinement fusion (ICF) sources conducted at

Sandia's Z pulsed power accelerator. In 2018, she joined the Lawrence Livermore National Laboratory, Livermore, CA, USA, to investigate and develop neutron measurements for ICF experiments conducted at the National Ignition Facility.

Matthew R. Weis received the B.S.E., M.S.E., and Ph.D. degrees in nuclear engineering and radiological sciences from the University of Michigan at Ann Arbor, Ann Arbor, MI, USA, in 2010, 2012, and 2015, respectively.

Since 2015, he has been with Sandia National Laboratories, Albuquerque, NM, USA, where he has been contributing modeling work to the inertial confinement fusion experiments on the Sandia's Z machine, the Omega and Omega-EP lasers, and the National Ignition Facility.



Eric C. Harding received the B.Sc. and Ph.D. degrees from the University of Michigan at Ann Arbor, Ann Arbor, MI, USA, under the guidance of Dr. P. Drake, in 2003 and 2010, respectively. His Ph.D. thesis was on hydrodynamic instabilities in high-energy density plasmas.

He led experiments at both Nike Facility, Naval Research Laboratory, Washington, DC, USA, and Omega Laser Facility, Laboratory for Laser Energetics, Rochester, NY, USA, that investigated the Kelvin–Helmholtz instability. He is currently a Staff

Member with Sandia National Laboratories, Albuquerque, NM, USA, where he is a Principal Investigator for inertial confinement fusion experiments on the Z machine and focused on developing advanced X-ray imaging and spectroscopy diagnostics.



Matthias Geissel received the Dipl.Phys. (U.S. equiv. M.S.) degree in physics and the D.rer.Nat. (U.S. equiv. Ph.D.) degree in natural sciences/physics from the Technische Universität Darmstadt, Darmstadt, Germany, in 1997 and 2002, respectively.

His scientific career has been focusing on the science of high-energy density states of matter with intense heavy ion beams and high-energy/ultraintense lasers. Since 2003, he has been a Staff Member with Sandia National Laboratories,

Albuquerque, NM, USA, where he has been predominantly working on laser–matter interaction with Z-Petawatt Facility and Z-Beamlet Facility. His current research interests include magneto-inertial fusion, laser–plasma instabilities, and plasma diagnostics.

Jeffrey R. Fein received the B.S. degrees in physics and mathematics from the University of Pittsburgh, Pittsburgh, PA, USA, in 2001, and the M.S.E. and Ph.D. degrees in nuclear engineering and radiological sciences from the University of Michigan at Ann Arbor, Ann Arbor, MI, USA, in 2013 and 2017, respectively.

Since 2017, he has been a Post-Doctoral Appointee with Sandia National Laboratories, Albuquerque, NM, USA, where he develops X-ray imaging diagnostics and studies laser–plasma interactions relevant to magneto-inertial fusion experiments on the Z machine.



Michael E. Glinsky received the Ph.D. degree in theoretical and computational plasma physics from the University of California at San Diego, San Diego, CA, USA, in 1991, under the guidance of T. O’Neil and M. Rosenbluth.

He was with the ICF Program, Lawrence Livermore National Laboratory, Livermore, CA, USA, for six years. He was involved in geophysics research (and research management) for 20 years. This included being the Chief Geoscientist for the Commonwealth Scientific and Industrial Research

Organisation, Kensington, WA, Australia, and an Adjunct Professor of physics with The University of Western Australia, Crawley, WA, Australia. For the past three years, he has been a Physicist with Sandia National Laboratories, Albuquerque, NM, USA, where he was involved in the research on inertial confinement fusion on the Z machine.

Dr. Glinsky’s thesis won the 1993 American Physical Society Award, for being the outstanding thesis in plasma physics.



Stephanie B. Hansen received the B.S. and Ph.D. degrees in physics and the B.A. degree in philosophy from the University of Nevada, Reno, NV, USA.

Since 2012, she has been a Visiting Associate Professor with Cornell University, Ithaca, NY, USA. She is currently a Distinguished Member of Technical Staff with the ICF Target Design Group, Sandia National Laboratories, Albuquerque, NM, USA, where she develops atomic, spectroscopic, equation-of-state, and transport models to help predict and diagnose the behavior of high-energy density plasmas. She is the Author and the Developer of the spectroscopic collisional-radiative atomic model nonlocal thermodynamic equilibrium spectroscopic modeling code, which is currently used at multiple institutions, and of MUZE, a self-consistent field code used for equation-of-state, scattering, and transport calculations.

Dr. Hansen was a recipient of the five-year Early Career Grant from the Department of Energy’s Office of Fusion Energy Sciences to study the atomic-scale behavior of materials at extreme conditions in 2014 and the Presidential Early Career Award for Scientists and Engineers in 2017.



Adam J. Harvey-Thompson received the M.Sci. and Ph.D. degrees from the Imperial College, London, U.K., in 2006 and 2010, respectively. His Ph.D. thesis was on novel, inverse wire array configurations to understand ablation dynamics and as a current switch.

From 2010 to 2012, he was a Post-Doctoral Researcher with the Imperial College, where he studied plasma ablation using optical Thomson scattering. Since 2012, he has been a Staff Member with Sandia National Laboratories, Albuquerque, NM,

USA, where he has studied argon gas puff Z-pinch and inertial confinement fusion on the Z machine and the Z beamlet laser.

Christopher A. Jennings received the M.Sci. degree in physics and the Ph.D. degree in computational plasma physics from the Imperial College, London, U.K., in 2005.

Since 2006, he has been with Sandia National Laboratories, Albuquerque, NM, USA, where he has been working on the computational modeling of pulsed power-driven experiments on the Z generator.



Ian C. Smith received the B.Sc. degree in physics with laser technology from University of Essex, Essex, U.K., in 1985.

He began his working career as a member of the Laser Team Atomic Weapons Establishment (AWE), Aldermaston, U.K., where he has been operating the HELEN laser system and leading this team by the early 1990s. From 1993 to 1996, he was with the Lawrence Livermore National Lab, Livermore, CA, USA, where he was involved in the National Ignition Facility scientific prototype, BEAMLET. He

returned to AWE and worked on the multipass cavity design for the HELEN upgrade, later used as the platform for the ORION laser. In 2000, he was assigned to Sandia National Laboratories, Albuquerque, NM, USA, to assist in relocating the BEAMLET laser to the Z pulsed power machine to form the Z-Backlighter Facility. In 2002, he became a Staff Member with Sandia, where he currently leads the operation of the Z-Backlighter Facility.



Daniel Woodbury received the B.S. degree in physics from Brigham Young University, Provo, UT, USA, in 2015.

He is currently enrolled in the Physics Ph.D. Program at the University of Maryland at College Park, College Park, MD, USA. His current research interests include relativistic laser-plasma interactions, laser-driven particle and light sources, mid-infrared ultrafast laser systems, nonlinear optics, and magneto-inertial fusion.

Dr. Woodbury was a recipient of the DOE NNSA Stewardship Science Graduate Fellowship, which has supported his research on intense ultrafast lasers and collaborative work at Sandia National Laboratories, Albuquerque, NM, USA.



David J. Ampleford (M'07–SM'14) received the M.Sci. and Ph.D. degrees from the Imperial College, London, U.K., in 2001 and 2005, respectively. His PhD thesis was on the 1-MA MAGPIE pulsed power generator for laboratory astrophysics modeling of proto-stellar jets.

In 2005, he joined Sandia National Laboratories, Albuquerque, NM, USA, where he is currently a Staff Member with the Radiation & Fusion Experiments Department. His current research interests include the magneto-inertial fusion science, the development of multi-keV radiation sources, and the diagnostic development.

Dr. Ampleford received the IEEE Nuclear and Plasma Sciences Society Early Achievement Award in 2014.

Thomas J. Awe received the Ph.D. degree in physics from the University of Nevada, Reno, NV, USA, in 2009.

After a post-doctoral appointment at the Los Alamos National Laboratory, Los Alamos, NM, USA, he joined Sandia National Laboratories, Albuquerque, NM, USA, in 2011. His current research interests include inertially confined plasmas for fusion and instability evolution on magnetically accelerated systems.

Gordon A. Chandler (M'98) received the Ph.D. degree in engineering applied science from the University of California at Davis, Davis, CA, USA, in 1988.

In 1988, he joined the Staff at Sandia National Laboratories, Albuquerque, NM, USA. His current research interests include inertial confinement fusion.

Mark H. Hess received the B.S. degrees in physics and mathematics from the University of Maryland at College Park, College Park, MD, USA, in 1997, and the Ph.D. degree in physics from the Massachusetts Institute of Technology, Cambridge, MA, USA, in 2002.

Since 2011, he has been a Staff Member with Sandia National Laboratories, Albuquerque, NM, USA, where he studies inertial confinement fusion and radiation sources at the Z Pulsed Power Facility. His current research interests include understanding the power flow in the Z machine experiments.



Derek C. Lamppa (M'15) received the B.S. degree in electrical engineering from New Mexico Tech, Socorro, NM, USA, in 2004, and the M.S. degree in electrical engineering from The University of New Mexico, Albuquerque, NM, USA, in 2010.

He is currently enrolled in the Ph.D. program at the Electrical and Computer Engineering Department, The University of New Mexico, where he has been researching the power flow in the magnetically insulated transmission lines in the Sandia's Z Machine. Since 2004, he has been a Staff Member with Sandia

National Laboratories, Albuquerque, NM, USA. His current research interests include the design of novel electromagnets for the premagnetization of magnetized liner inertial fusion fuel, electromagnetic launch, and fast-closure shutters. He is also developing new diagnostics to study the influence of magnetically insulated transmission line plasma dynamics on current loss during Z experiments.



Clayton E. Myers received the B.S. degree in engineering physics from Cornell University, Ithaca, NY, USA, in 2007, and the M.A. and Ph.D. degrees in astrophysical sciences from Princeton University, Princeton, NJ, USA, in 2009 and 2015, respectively.

From 2015 to 2017, he was a Research Physicist with the Princeton Plasma Physics Laboratory, where he was studying magnetohydrodynamic stability and disruption phenomena on the National Spherical Torus Experiment Upgrade (NSTX-U).

Since 2017, he has been a Research Physicist with Sandia National Laboratories, Albuquerque, NM, USA, where he studies inertial confinement fusion and high-energy density science on the Z Pulsed Power Facility.

Dr. Myers received the 2018 LAD Dissertation Prize from the Laboratory Astrophysics Division of the American Astronomical Society, for his thesis research studying the magnetohydrodynamic equilibrium and eruption of solar-relevant magnetic flux ropes in the laboratory.

Carlos L. Ruiz received the Ph.D. degree in experimental nuclear physics from The University of Kansas, Lawrence, KS, USA, in 1974.

He then spent the next seven years on the Faculty at Louisiana State University, Baton Rouge, LA, USA. In 1981, he joined Sandia National Laboratories, Albuquerque, NM, USA, where he has contributed solely to the development of nuclear-based diagnostics primarily used in inertial confinement fusion experiments in the Pulsed Power Directorate and, in particular, the Z Facility.

Adam B. Sefkow (M'17) received the Ph.D. degree in plasma physics from Princeton University, Princeton, NJ, USA, in 2007.

In 2016, he was a Designer of pulsed power loads on the Z machine during his tenure at Sandia National Laboratories, Albuquerque, NM, USA. Since 2016, he has been an Assistant Professor of mechanical engineering and physics with the University of Rochester, Rochester, NY, USA.

Dr. Sefkow received the Department of Energy Early Career Research Program Award in 2017.

Jens Schwarz received the B.S. degree in physics from the University of Würzburg, Würzburg, Germany, the M.S. degree in physics from The University of New Mexico, Albuquerque, NM, USA, and the Ph.D. degree in physics from the University of Jena, Jena, Germany, in 2003, for his work on UV short-pulse laser propagation in air.

Since then, he has been a Laser Scientist for the Z-PW laser at the Z-Backlighter Facility, Sandia National Laboratories, Albuquerque, NM, USA, and a Principal Investigator at the Sandia's Z Pulsed Power Accelerator.



David A. Yager-Elorriaga (M'13) received the B.A. degree in physics and mathematics with a minor in Spanish from the Gettysburg College, Gettysburg, PA, USA, in 2010, and the M.S.E. and Ph.D. degrees in nuclear engineering and radiological sciences from the University of Michigan at Ann Arbor, Ann Arbor, MI, USA, in 2013 and 2017, respectively.

Since 2017, he has been a Staff Member with Sandia National Laboratories, Albuquerque, NM, USA, where he studies inertial confinement fusion and high-energy density physics on the Z machine.

Dr. Yager-Elorriaga received the National Science Foundation Graduate Fellowship in 2012 to investigate magneto Rayleigh–Taylor instability in Z-pinch.

Brent Jones (M'06) received the B.S. degree in physics from the University of Washington, Seattle, WA, USA, in 1997, and the Ph.D. degree in physics from Princeton University, Princeton, NJ, USA, in 2002.

In 2002, he joined Sandia National Laboratories, Albuquerque, NM, USA, where he has been focusing on Z-pinch physics and X-ray sources and currently managing the High Energy Density Experiments Department, performing research at the Z Pulsed Power Facility.

Dr. Jones was the recipient of the IEEE NPSS 2012 Early Achievement Award.



John L. Porter received the B.S. degree in physics from the California Institute of Technology, Pasadena, CA, USA, in 1981, and the Ph.D. degree in plasma physics from The University of Texas at Austin, Austin, TX, USA, in 1985.

In 1985, he joined Sandia National Laboratories, Albuquerque, NM, USA, as a Member of Technical Staff, and has been a Technical Manager with Sandia since 1997. His current research interests include inertial confinement fusion, Z-pinch, magnetized plasmas, and developing high-speed X-ray imaging

and spectroscopic instruments to study the dynamics of high-energy density plasmas.

Dr. Porter received the Lockheed Martin NOVA Award in 2002 and the R&D100 Award in 2016.



Kyle J. Peterson (M'15) received the bachelor's degree in physics from North Park University, Chicago, IL, USA, in 1998, and the Ph.D. degree in physics from The University of Tennessee, Knoxville, TN, USA, in 2003.

He is currently the Manager of the Radiation and Inertial Confinement Fusion Target Design Department, Sandia National Laboratories, Albuquerque, NM, USA. In this role, he directs Sandia's theoretical and computational efforts in inertial confinement fusion and radiation effects target design for Sandia's Z Facility.



Ryan D. McBride (M'00) received the Ph.D. degree from Cornell University, Ithaca, NY, USA, in 2009.

He conducted experimental research on wire-array Z-pinch implosions using the 1-MA COBRA Pulsed Power Facility at Cornell University. From 2008 to 2016, he was with Sandia National Laboratories, Albuquerque, NM, USA, where he held appointments as a Staff Physicist and the Department Manager. At Sandia, he conducted research in nuclear fusion, radiation generation, and high-pressure material properties using the 25-MA Z Pulsed Power

Facility. He is currently an Associate Professor with the Department of Nuclear Engineering and Radiological Sciences, University of Michigan at Ann Arbor, Ann Arbor, MI, USA. His research is conducted primarily within the Plasma, Pulsed Power, and Microwave Laboratory, University of Michigan, which includes two linear transformer driver facilities: MAIZE (Michigan Accelerator for Inductive Z-pinch Experiments; ~ 1 MA, ~ 100 ns) and BLUE (Bestowed LTD from the Ursa-minor Experiment, where LTD is linear transformer driver; ~ 150 kA, ~ 100 ns). His current research interests include plasma physics, nuclear fusion, radiation generation, pulsed power technology, plasma diagnostics, and the dynamics of magnetically driven, cylindrically imploding systems. Most recently, his research has been focused on both experimental and theoretical studies of magnetized liner inertial fusion, which is currently one of the United States' three mainline approaches to studying controlled inertial confinement fusion in the laboratory.

Gregory A. Rochau received the B.S. degree in physics from Drake University, Des Moines, IA, USA, in 1998, and the Ph.D. degree in engineering physics from the University of Wisconsin–Madison, Madison, WI, USA, in 2003.

He is currently the Manager of the Radiation and Fusion Experiments Department, Sandia National Laboratories, Albuquerque, NM, USA. He plays leading roles in shot planning and execution on the Z Facility and in the U.S. National efforts in magnetic direct drive inertial confinement fusion (ICF) and transformative diagnostic development for the U.S. ICF facilities: NIF, Z, and Omega.



Daniel B. Sinars (M'04–SM'17) received the B.S. degree from The University of Oklahoma, Norman, OK, USA, in 1996, and the Ph.D. degree from Cornell University, Ithaca, NY, USA, in 2001.

He is currently the Senior Manager of the Radiation and Fusion Physics Group, Sandia National Laboratories, Albuquerque, NM, USA. He is responsible for leading and coordinating the Sandia's research activities in the Inertial Confinement Fusion Program as the Sandia's Deputy ICF Executive.

He leads the development and application of intense X-ray and fusion neutron sources driven by magnetic compression, as well as the advanced X-ray imaging and spectroscopy diagnostics needed to support this research. His current research interests include the experiments using the 80-TW, 20-MJ Z Pulsed Power Facility, as well as the adjacent Multi-kJ, 2-TW Z-Beamlet Laser Facility, Sandia National Laboratories.

Dr. Sinars is a fellow of the American Physical Society. He received the 2007 IEEE Nuclear and Plasma Sciences Society Early Achievement Award, the 2011 Department of Energy Early Career Research Program Award, and the 2011 Presidential Early Career Award for Scientists and Engineers.